Ubiquitous and continuous propagating disturbances in the solar corona

Morgan, Huw; Hutton, Joseph

Published in:
Astrophysical Journal

DOI:
10.3847/1538-4357/aaa4b9

Publication date:
2018

Citation for published version (APA):
Morgan, H., & Hutton, J. (2018). Ubiquitous and continuous propagating disturbances in the solar corona. *Astrophysical Journal*, *853*(2), [145]. https://doi.org/10.3847/1538-4357/aaa4b9

Draft version December 30, 2017
Typeset using LaTeX **preprint** style in AASTeX61

UBIQUITOUS AND CONTINUOUS PROPAGATING DISTURBANCES IN THE SOLAR CORONA

Huw Morgan[1] and Joseph Hutton[1]

[1]*Institute of Mathematics, Physics & Computer Science, Aberystwyth University, Aberystwyth, Ceredigion, Cymru, UK, SY23 3BZ*

(Received December 30, 2017; Revised December 30, 2017; Accepted December 30, 2017)

Submitted to ApJ

ABSTRACT

A new processing method applied to Atmospheric Imaging Assembly/Solar Dynamic Observatory observations reveals continuous propagating faint motions throughout the corona. The amplitudes are small, typically 2% of the background intensity. An hour's data is processed from four AIA channels for a region near disk center, and the motions characterized using an optical flow method. The motions trace the underlying large-scale magnetic field. The motion vector field describes large-scale coherent regions that tend to converge at narrow corridors. Large-scale vortices can also be seen. The hotter channels have larger-scale regions of coherent motion compared to the cooler channels, interpreted as the typical length of magnetic loops at different heights. Regions of low mean and high time variance in velocity are where the dominant motion component is along the line of sight due to a largely vertical magnetic field. The mean apparent magnitude of the optical velocities are a few tens of km s^{-1}, with different distributions in different channels. Over time, the velocities vary smoothly between a few km s^{-1} to 100 km s^{-1} or higher, varying on timescales of minutes. A clear bias of a few km s^{-1} towards positive x-velocities is due to solar rotation and may be used as calibration in future work. All regions of the low corona thus experience a continuous stream of propagating disturbances at the limit of both spatial resolution and signal level. The method provides a powerful new diagnostic tool for tracing the magnetic field, and to probe motions at sub-pixel scales, with important implications for models of heating and of the magnetic field.

Keywords: methods: data analysis — Sun: corona — Sun: magnetic fields — Sun: oscillations — techniques: image processing

Corresponding author: Huw Morgan
hmorgan@aber.ac.uk

1. INTRODUCTION

Large-scale closed-field regions of the corona associated with sunspots contain hot, high-density plasma (T$\gtrsim$2MK) (Habbal et al. 2010a; Morgan et al. 2013; Del Zanna 2013), open-field regions are generally colder and low-density (T$\lesssim$1.1MK) (Hahn et al. 2011; David et al. 1998; Habbal et al. 2010b), and in between is the largely closed-field quiet corona (T$\sim$1.4MK) (Mackovjak et al. 2014; Hahn & Savin 2014). The energy budget of the quiet chromosphere (corona) is $\sim$4000 (300) Wm^{-2}, with active regions requiring 2×10^4 (10^4) Wm^{-2} (Withbroe & Noyes 1977). Magnetoacoustic waves cannot provide the required power (Carlsson et al. 2007). Recent studies disagree whether Alfven waves can provide sufficient energy(De Pontieu et al. 2007; McIntosh et al. 2011; Thurgood et al. 2014). The movement of kilogauss flux tubes creates stress and reconnection at small-scale current sheets - this is the nanoflare model of heating (Parker 1988; Klimchuk 2006; Hansteen et al. 2015). There are reasons to support the bulk heating of plasma in the chromosphere, some proportion of which flows to the corona to maintain high temperatures, although the debate has not been settled (De Pontieu et al. 2014; Aschwanden et al. 2007; Klimchuk & Bradshaw 2014; Bradshaw & Klimchuk 2015). Some heating theories rely on sophisticated models while others represent general concepts (Parnell & De Moortel 2012). Important effects governing heating operate at scales beyond the spatiotemporal resolution of current and planned observations thus indirect observational methods are required, such as power laws in order to estimate the contribution at unresolved scales (e.g. Aschwanden et al. 2016), or the nature of flows along loops (e.g. Schrijver 2001; Mendoza-Briceño & Erdélyi 2006; Antolin et al. 2010; Krishna Prasad et al. 2017).

Recent observational advances have opened a window into activity at fine spatial (<arcsec) and temporal ($\sim$seconds) scales, enabling detailed study of oscillations, small-scale brightenings and flows. These observables provide an opportunity for meaningful constraints on heating models. A major problem facing the field is to disentangle the role and connection between the myriad small-scale events that may manifest differently in different types of observations. Consideration of availability of wave energy supports wave heating in the chromosphere, thus observations of coronal waves/flows (or *coronal propagating disturbances*, CPD (De Moortel 2009)) are interpreted as energy input from the lower atmosphere. Recent efforts are linking photospheric drivers and shocks generated by slow-mode chromospheric waves with CPDs (e.g. Langangen et al. 2008). The best candidate for transporting this energy are transition region/low coronal dynamic fibrils (or type I spicules) (e.g. De Pontieu et al. 2005, 2007; Skogsrud et al. 2016), and type II spicules (e.g. Pant et al. 2015; De Pontieu et al. 2011; Henriques et al. 2016). Spicules are ubiquitous in the transition region/low corona, and are a manifestation of energy injection from the chromosphere to the corona. The mass and energy flux due to spicules make them an important candidate to maintain high coronal temperatures (Raouafi et al. 2016; Tsiropoula et al. 2012; Sterling 2000). The connection between chromospheric shock waves, spicules and CPD remains unclear (e.g. Bryans et al. 2016). There is also confusion over the wave or flow nature of CPDs based on observational limitations and the limited number of current studies (Verwichte et al. 2010; De Moortel et al. 2015).

There is no comprehensive study of small-scale waves and flows over a long time period, and a systematic statistical distinction of small-scale activity within different regions of the solar atmosphere. Current studies are generally limited to limited regions over relatively short timescales, and often depend on manual input for detection and tracking. This has two drawbacks - findings from one case study cannot represent the whole picture, and a statistical approach may not be possible. Many

studies link chromospheric or transition region activity with coronal features, for example, linking slow-mode chromospheric waves (e.g. Langangen et al. 2008), with CPDs. The features/events are placed in the context of large-scale coronal features through the particular properties of the case study, for example, fan-shaped regions at the periphery of active regions are prime sites to observe wave or periodic flow activity (e.g. De Moortel 2009). Statistical studies contain important results, for example, a preference for 3-minute oscillations above sunspot loops, and 5-minute in plage regions (e.g. De Moortel et al. 2002).

To causally or statistically link dynamic phenomena between different layers in the solar atmosphere requires information of the coronal magnetic field, yet this all-important structure cannot be measured directly. Advanced ground-based spectropolarimetric measurements leading to estimates of the coronal field are restricted to small regions, and are subject to line-of-sight summation (Lin et al. 2004; Kleint & Gandorfer 2017), and direct routine observations across broad regions of the corona remains a long-term goal. Global MHD models extrapolate the observed photospheric magnetic field to the corona (e.g. Wu & Dryer 2015; Feng et al. 2011; Feng & Xiang 2013) using various approaches. The success of MHD models depends critically on the specification of the boundary conditions at the coronal base, and several assumptions are used. Despite the success of model magnetic field extrapolations, they lack observational constraint, and their accuracy is most often judged through a qualitative comparison with, for example, EUV or white light coronal images. Any additional quantiative observational constraint on the coronal magnetic field is therefore valuable. One approach is to use observed structures in EUV observations as a spatial constraint on magnetic extrapolation, for example through the automated tracing of curvi-linear features (Aschwanden et al. 2016).

Image processing is important in solar physics to help reveal structure and dynamic phenomena. Methods for spatial enhancement in EUV images include wavelet-based techniques (Stenborg & Cobelli 2003), Multiscale Gaussian Normalization (MGN, Morgan & Druckmüller 2014) and Noise Adaptive Fuzzy Equalization (Druckmüller 2013). For revealing or enhancing dynamic events, time-differencing is often used. This can be a running difference (subtracting a previous image from the image of interest), or a base difference (subtracting an initial image from a subsequent series). Running or base ratios can also be used rather than subtraction. An effective method is to subtract a running mean or median (calculated for a sliding window of fixed time, Plowman 2016). Optical flow methods, including local correlation tracking (Fisher & Welsch 2008) or other more advanced approaches (Asensio Ramos et al. 2017), are commonly used in solar physics to track photospheric motions. They are sometimes used in a coronal context to track certain dynamic events (e.g. Li et al. 2012).

This work presents a simple new image processing technique in section 2 with the aim of revealing faint motions, with results presented in section 3. The results of applying an adapted optical flow method to track the faint flows is presented in section 4, with the details of the method reserved for Appendix 1. An analysis of the effect of certain method parameters on the results is given in section 5. Section 6 shows how the motion tracking results change over time. Other aspects of the results are discussed in detail in section 7, along with some interpretation. Conclusions are in section 8.

2. TIME NORMALIZATION: METHOD

The Atmospheric Imaging Assembly (AIA, Lemen et al. (2012)) instrument aboard the Solar and Dynamic Observatory (SDO, Pesnell et al. (2012)) collects high spatial resolution images ($\sim$0.6″) of the whole solar disk in multiple wavelength channels at high temporal resolution ($\sim$12s). The high

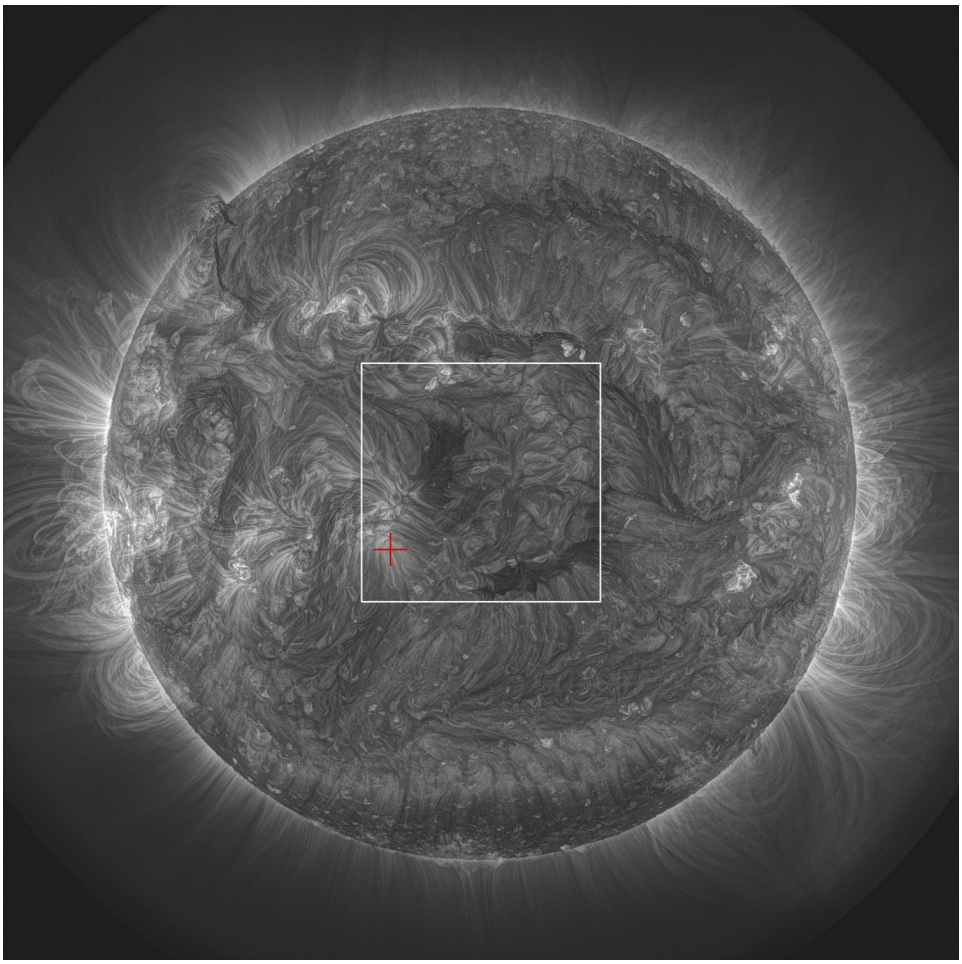

Figure 1. Example AIA image taken in the 193Å channel, for date 2015/03/21 18:27. This image has been processed by Multiscale Gaussian Normalization (MGN, (Morgan et al. 2012)) in order to enhance fainter structures at smaller spatial scales. The 193Å channel is dominated by emission from Fe XII, and has a temperature response strongly peaked at 1.6MK. The red cross indicates the position of a pixel, the time series of which is used as an example in the method. The boxed region is used to illustrate initial results.

resolution and regularity of the observations are well suited for a study of dynamic characteristics. AIA data collected bewteen 2015/03/21 18:00 to 19:00 in the 193Å channel are used as an example throughout this section. Figure 1 shows an example of an observation in this channel. The white boundary indicates a region which will be analyzed in detail, and the red cross indicates a single pixel from which the signal time series will be used to illustrate the method.

The method is based on a sliding time window of consecutive observations at the highest observation cadence. Figure 2a shows the time-varying signal for the pixel indicated in figure 1, over a time range of 15 minutes. This signal is convolved with a narrow Gaussian kernel of width (standard deviation) 2 time steps (or at the standard 12s observational cadence, 24s, FWHM=56s). This step reduces noise at high frequencies, whilst preserving the variations of interest at mid and low frequencies. The smoothed signal is shown as a solid black line in figure 2a. The weighted mean $\bar{S}$ and standard deviation σ of the smoothed signal is calculated for the 15 minute period, using a wide Gaussian weighting of width (standard deviation) 150s (FWHM=353s), centered on the central observation of the 15 minute time series, shown as red lines in figure 1. The central observation S is then normalized

to give the processed signal S' by

$$S' = \frac{S - \bar{S}}{\sigma + c}. \quad (1)$$

Pixels of low signal have a small σ, and including a small constant c to the denominator of equation 1 helps suppress amplification of noise in the final processed image.

The choice of width for the wide Gaussian kernel does have some impact on results, as will be shown in section 5. The choice of 150s used here and throughout the results is discussed in that section. For the narrow kernel, the width of 24s is based on a quantitative visual inspection of final images. Using a kernel narrower than 24s results in noisier images, with less coherence in the observed motion. Therefore we have minimized the width of this kernel whilst still maintaining clear coherent motions in the resulting processed images.

At a cadence of 12s, the 15 minute time window requires loading a datacube of 75 images. Once an image is processed, the 15-minute sliding window is incremented in time by one time-step, and the process repeated. The dominant factor in computational time is the reading of the image files. Initializing the process requires loading ∼75 images into memory. Each subsequent time-step requires discarding the first image in the datacube and loading a new image at the end of the datacube, thus once the datacube is initialized the process is fairly efficient. Computational time can be reduced by binning the image to a coarser grid, or by processing smaller regions. In figure 2a, the mean $\bar{S}$ and standard deviation ($\pm\sigma$) are shown as red solid and dotted lines respectively. The final time-normalized signal S' is shown in figure 2b.

3. TIME NORMALIZATION: RESULTS

Figure 3 is a high-resolution example of a time-normalized image from the 193Å channel, side-by-side with an MGN image to provide context. Viewing a single image is not useful: it is important to view the accompanying movie to visualize the motions. The time-normalization is crucial to reveal these faint motions. Without normalization, the image is dominated by the spatial variation in intensity between regions and any method to characterize small, faint motions is dominated by the spatial, rather than temporal, variations. Through time-normalization, structural context is mostly lost, yet coherent motions are revealed throughout all on-disk regions. Propagating disturbances (PD) abound across the whole disk. Following sections will characterize these motions, yet the most important result is the presence of PDs everywhere. In the movie, the MGN context images in the left panel show no evidence of the underlying faint motions revealed by the time normalization.

Figure 4 shows the same time-normalized full-disk images in four different AIA channels. Again, it is important to view the accompanying movie. In the hotter, high-signal channels (171 and 193Å), faint off-limb motions are revealed, particularly above the poles. PDs are also revealed along large off-limb equatorial loops. Motions in the 211Å channel are similar to those in the 193Å, albeit with reduced signal off the limb. Motions in the 304Å channel are smaller-scale and less coherent than in the hotter channels. For example, the most obvious and coherent motions in the 193 and 211Å channels are along field lines emanting from bright (active) regions. These are not obvious in the 304Å channel, where motions are small-scale and are similar across both quiet and active regions. The 171Å channel shows coherent motions in some linear structures (e.g. emanating from active regions), but less so in the quiet Sun compared to the hotter channels. This is likely due to the domination of 171Å emission from lower-lying loops. Similarly for the cool 304Å channel, the motions are from

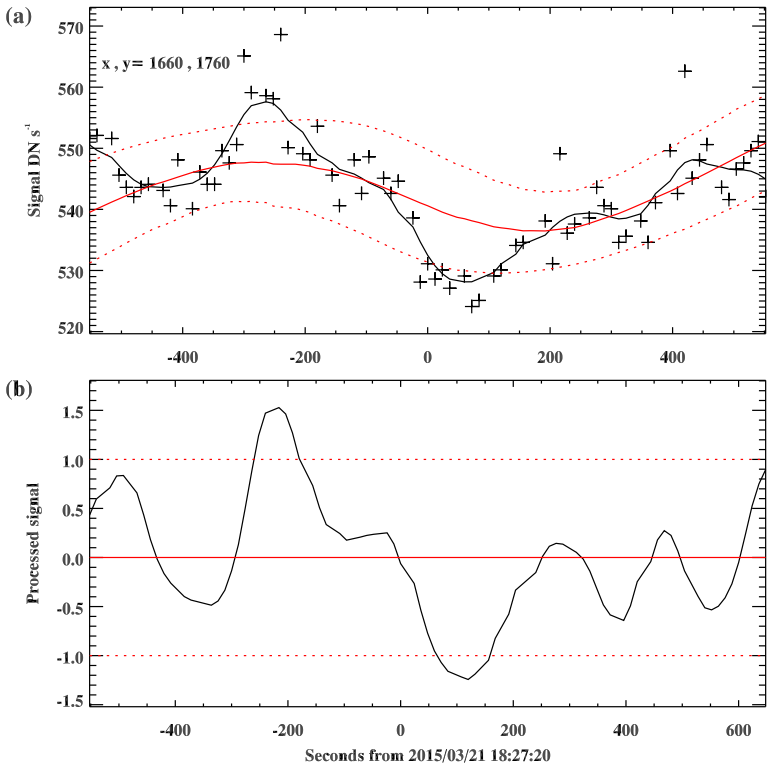

Figure 2. (a) The crosses show the time series over a 15 minute range (for the pixel shown by a red cross in figure 1). The black line shows the time-smoothed signal (convolution with a narrow kernel in time). The solid red line shows the slow variation in the signal (convolution with a wide kernel in time). The dotted red lines show the ±1 standard deviation from the mean (calculated over the wide sliding time-window). (b) The processed signal, after the normalization of equation 1.

the lowest corona, and fail to show coherence across large spatial scales since they do not propagate along large-scale structures.

Figure 5 shows detail of the central disk region, indicated by a white box in figure 1. These high-resolution images show a myriad of faint, complex motions. In the 304Å channel, these motions are small-scale and highly complex. The hotter 193 and 211Å images show more coherent motions that seem to trace the magnetic field structures seen in the non-time-processed images. Most clear are a series of brightness enhancements moving outwards from the bright region in the lower left part of the images, indicated by the red contour in the 193Å image. Some isolated regions seem to show coherent rotation in the 193Å and 211Å channels, most clearly in the region bounded by the green contour. This rotation is not apparent in the cooler channels.

Figure 6 shows distance-time plots along four selected paths through the original intensity images of the central disk region from the 193Å channel, along with the equivalent time-normalized values. For all four paths, immediately apparent in the time-normalized distance-time plots are enhancements that propagate along each path (or segment of the path) in time. A few of the brightest enhancements can also be faintly seen in the original intensity plots. The original intensity plots are dominated by spatial variations in intensity which prevent the visualisation of the faint propagating disturbances. The spatial variations are removed by time normalization, thus revealing the faint disturbances. For example, figure 6d shows a path which begins near a small active region, and traces

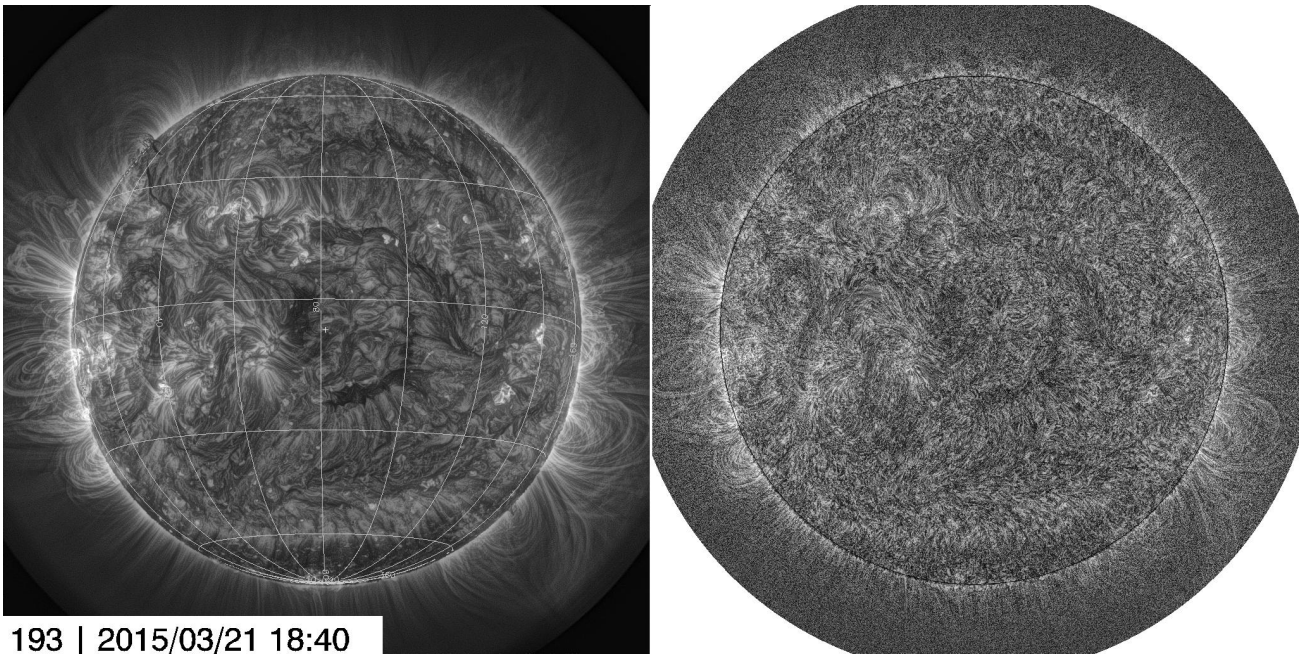

Figure 3. A pair of full-disk images observed by the AIA/SDO 193Å channel during 2015/03/21 18:40. The left panel shows an MGN-processed image, with Carrington co-ordinates, and the right panel shows the time-normalized image gained using equation 1. It is essential to view the accompanying online animation in order to visualize the motions.

a linear structure (loop) out from the active region to a distance of $\sim 0.1 R_\odot$ (path b). In the original intensity distance-time plot, the contrast of the values is dominated by the intensity decrease along the path with increasing distance from the active region. This spatial intensity gradient is removed by time normalization. Furthermore, any change in intensity of enhancements (or amplitude of disturbance) along a path is normalized by the image processing, allowing a better visualization of their propagation. The yellow dashed lines in the time-normalized plots have a gradient corresponding to 60 km s^{-1}, comparable to the slope of the brightest propagating disturbances. A detailed analysis of velocities is made in the following section.

The most prominent propagating disturbances appear every few minutes along each path. Two positions S0 and S1, separated by around 5000km, are chosen along path b. These two points are shown in figure 6e. The time series at these two positions is shown in figure 7a. The signals are very similar in profile, with the S1 signal consistently around 20 DN/s lower than at S0, being further from the active region. The autocorrelation of the S0 time series, and the cross-correlation between S0 and S1 is shown in figure 7b, and are not particularly interesting. In contrast, the time-normalized signal at the two positions shown in figure 7c reveal a clear correlation and lag. The autocorrelation of the time-normalized signal at S0 show secondary peaks at around ± 8 minutes, showing that the signal is varying on this timescale. The cross-correlation between S0 and S1 is strong ($\sim 70\%$) at a lag of 36s.

4. THE LK METHOD AND TRANSLATIONAL VECTOR FIELDS

The Lucas-Kanade (LK) method is widely used in the field of optical flow analysis (Lucas & Kanade 1981). Appendix 1 describes and demonstrates a LK method which we have adapted for use on the time-normalized AIA images. The LK method is applied to around 300 consecutive image pairs

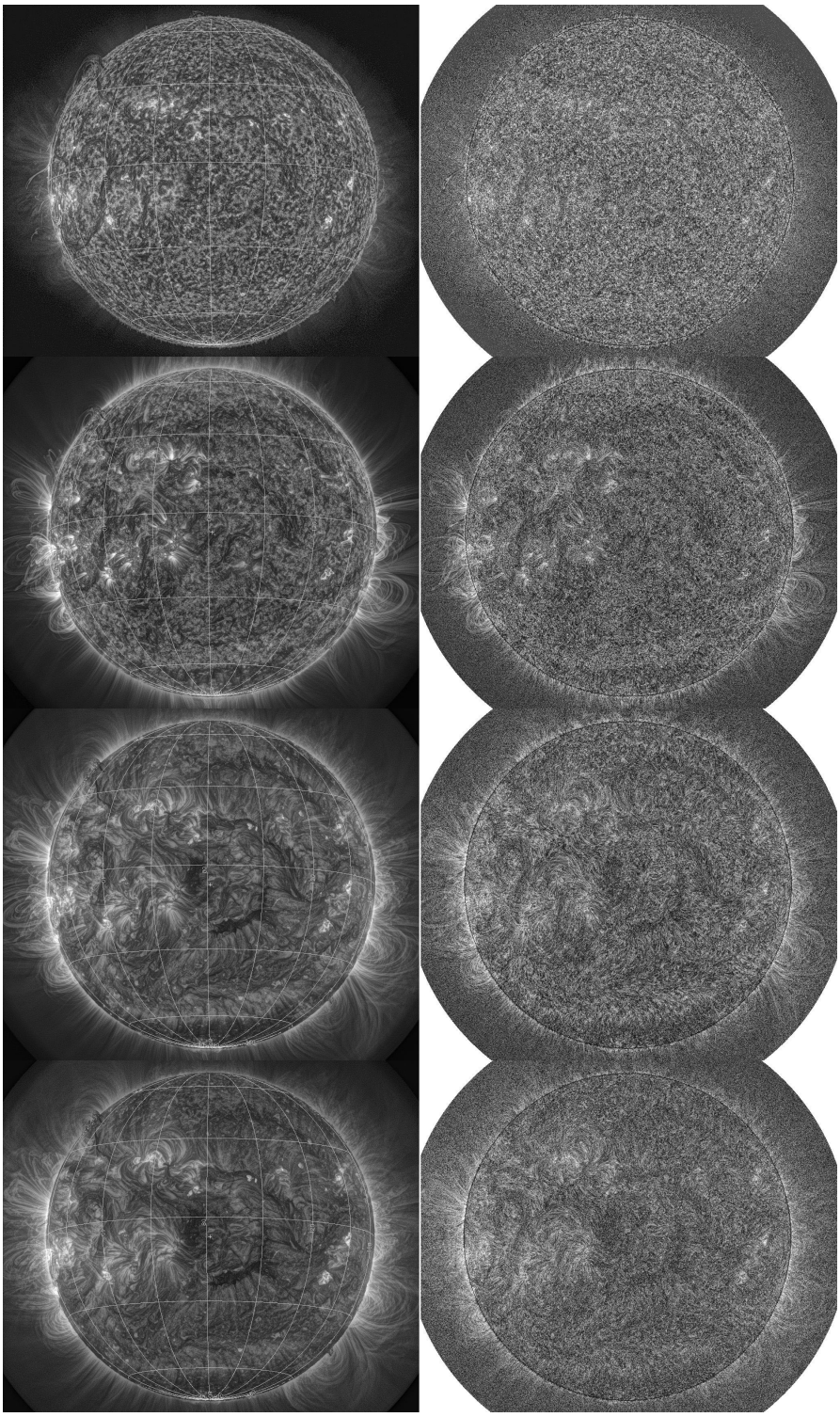

Figure 4. Four pairs of full-disk images corresponding to AIA/SDO channels 304, 171, 193 and 211Å (top to bottom) and time 2015/03/21 18:46. For each pair, the left panel shows an MGN-processed image and the right panel shows the time-normalized image gained using equation 1. It is essential to view the accompanying online animation in order to visualize the motions.

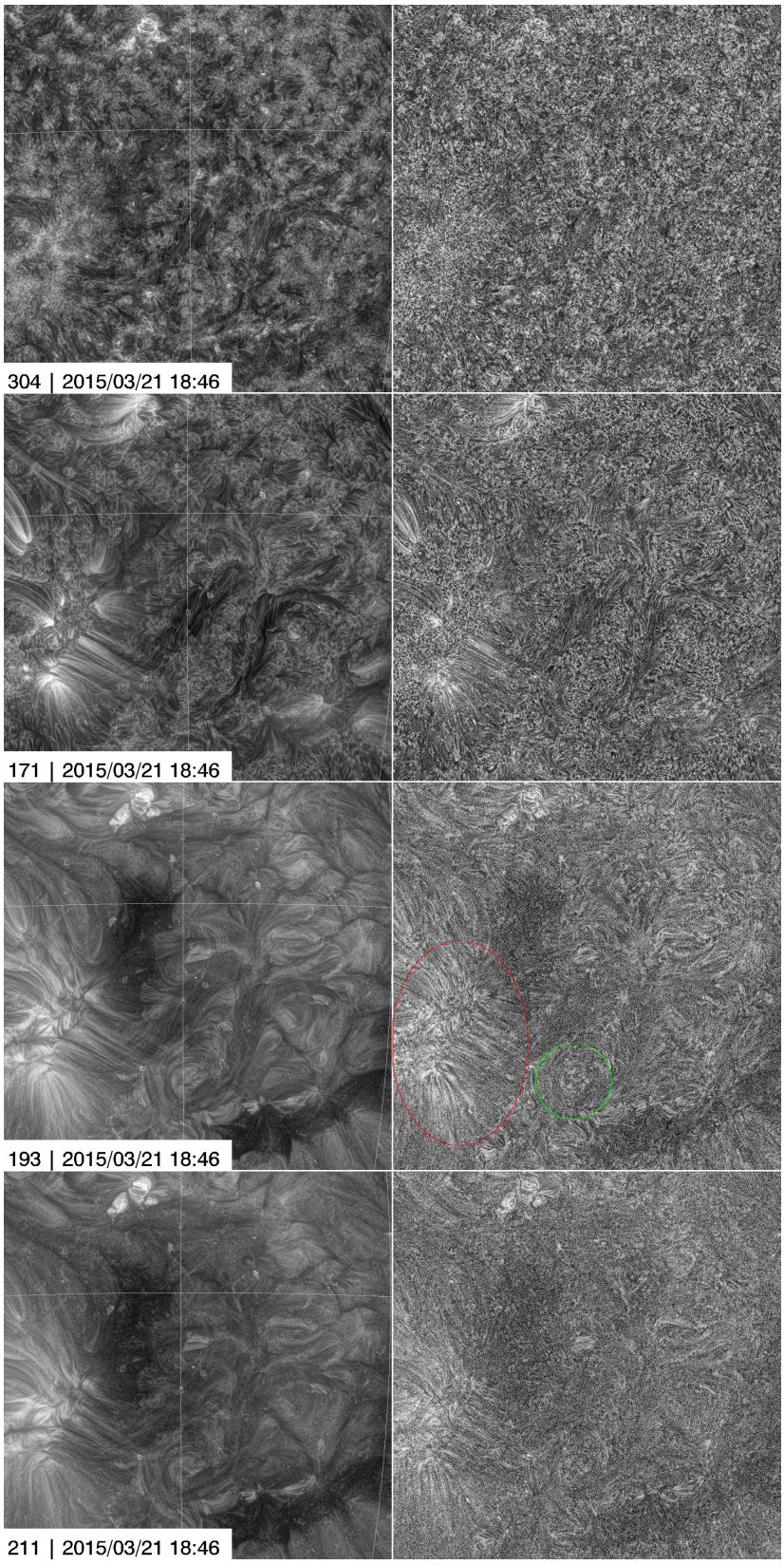

Figure 5. As figure 4, but showing the central disk region indicated by a white bounded box in figure 1. The red and green-bounded regions in the 193Å panel are referred to in the text. It is essential to view the accompanying online animation in order to visualize the motions.

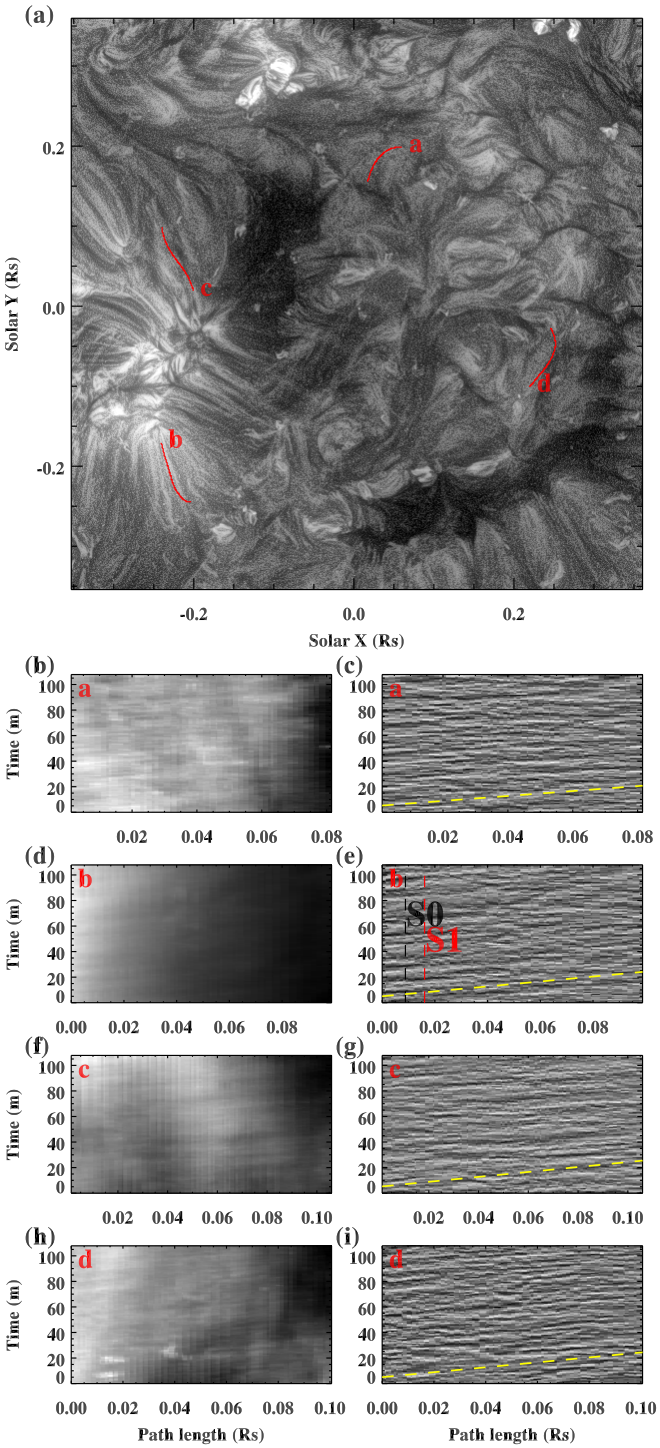

Figure 6. (a) 193Å intensity image of the disk center region, with four paths shown in red, labelled a-d. (b)-(i) Distance-time plots showing the original 193Å intensity (left column) and the time-normalized values (right column) for each of the four paths (as indicated a-d in each panel). The yellow dashed lines in the right column show a gradient corresponding to 60 km s^{-1}. The vertical black and red dashed lines labelled S0 and S1 in panel (e) shows the two positions along path b where time series are plotted in figure 7.

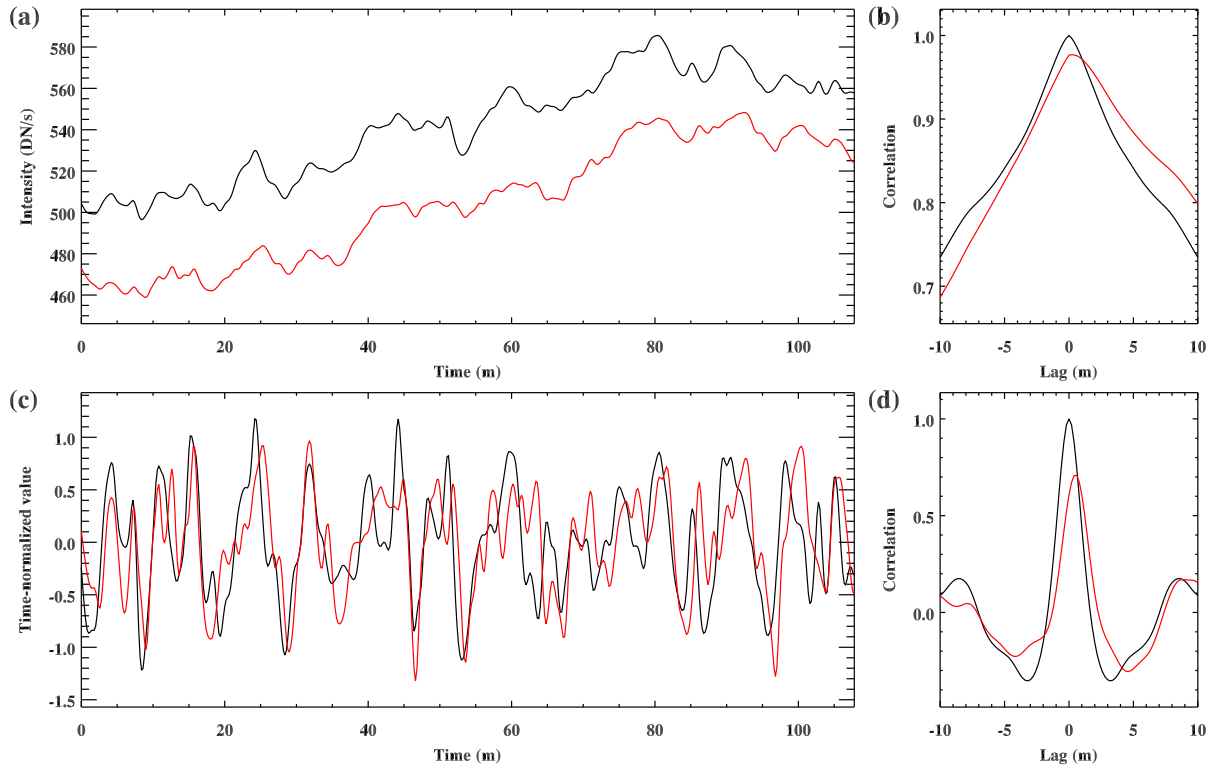

Figure 7. (a) Time series of 193Å intensity at the two positions S0 (black) and S1 (red) along path b, as shown by the vertical lines in figure 6e. (b) Autocorrelation of the signal at S0 (black), and cross-correlation of the signal at S0 and S1 (red). (c), (d) As (a) and (b), but for the time-normalized series.

(between 18:20 and 19:20UT on 2015/03/21) of the central disk region in four AIA channels: 304, 171, 193 and 211Å. For all pixels in each image pair, the local vector that describes the translation, or coherent movement of local structures between the consecutive time steps is found. This is a translation in the image plane which can be described as a velocity field (i.e. the pixel, or sub-pixel, shift in the x and y dimensions of the image per time step). In this section, the optical flow results are described as a 'translational field' - how this field relates to apparent motion and velocities of plasma in the low corona is discussed later. The translational fields for each channel are averaged over the hour period using a weighted average based on the vector direction in the image plane. This averaging is based on the assumption that over the hour time period, any persistent motions in the corona should not change direction abruptly in time, or at least there should be a preferred or dominant direction to propagating enhancements. The steps are: (1) The initial median direction is determined, (2) The difference between the median and each direction in time is determined, (3) An array of weights is created based on a Gaussian function of the direction differences. Using this weighting, the time-averaged x and y pixel translations are determined, on which the final translational field is based. Thus timesteps where the local translational direction is close to the median direction contribute more to the final value than timesteps which vary greatly from the median. These time variations are discussed in more detail in a following section.

The resulting translational vector field for the 193Å channel is shown in detail in figure 8, with smaller maps for all four channels shown in figure 9. This representation of the field confirms what we can see from the movies: the hotter channels show motions which are coherent over larger spatial

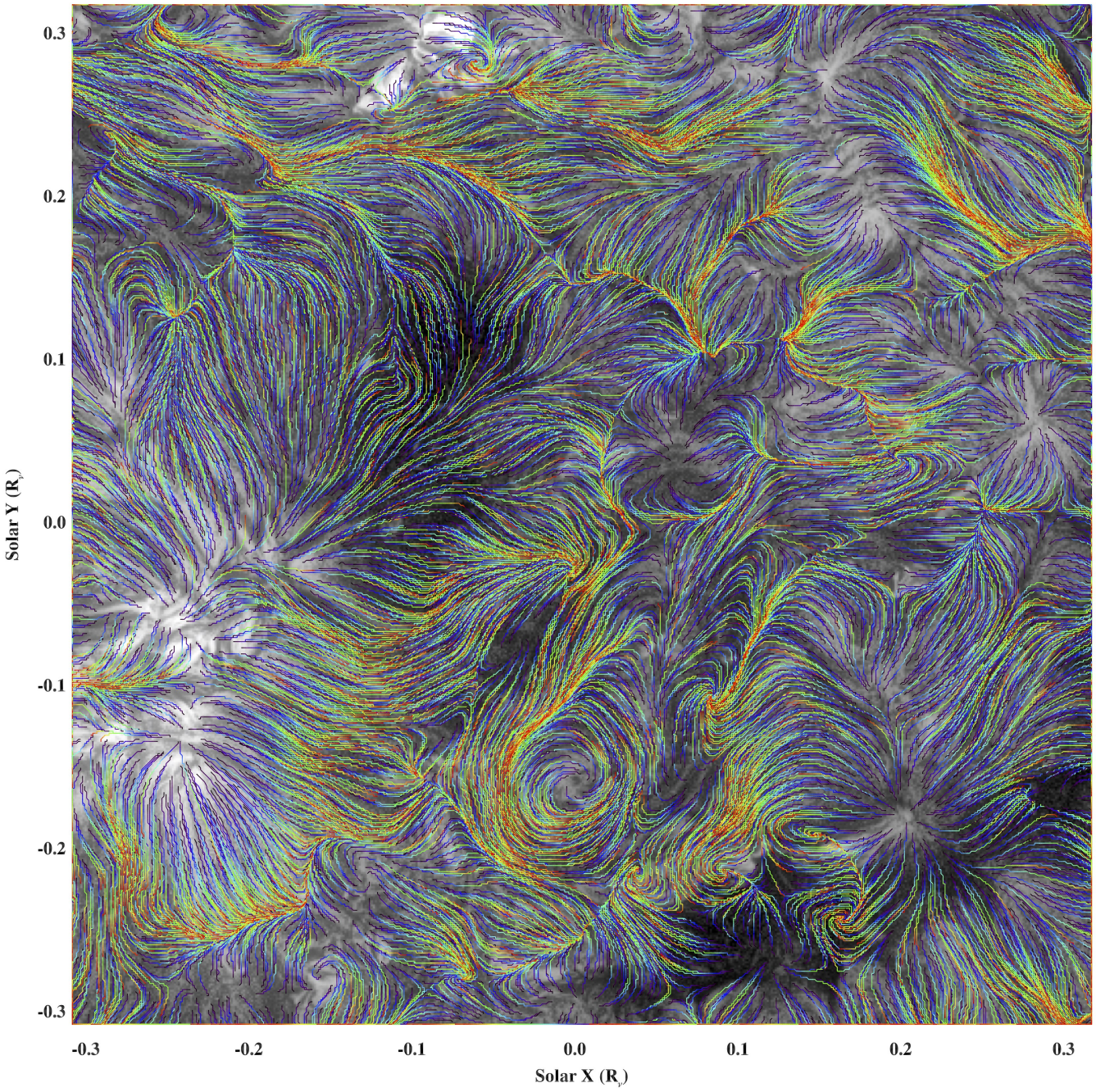

Figure 8. The translational field gained from applying the LK-method to the time-normalized images in the AIA 193Å channel. The background image is an MGN image. The field lines are traced from a grid of several hundred start points. Each line traces the direction of the flow field, with a local path length dictated by the local field magnitude. To visualise the flow direction, each line starts in blue then proceeds from purple, green, yellow, and end in red.

scales than the cooler channels, with the most coherent linear motions along magnetic structures outwards from brighter regions. The translational fields also clearly show several regions of rotation, or vortices, particularly in the hotter 193 and 211Å channels, with the most clear example above the green-circled region shown in figure 5.

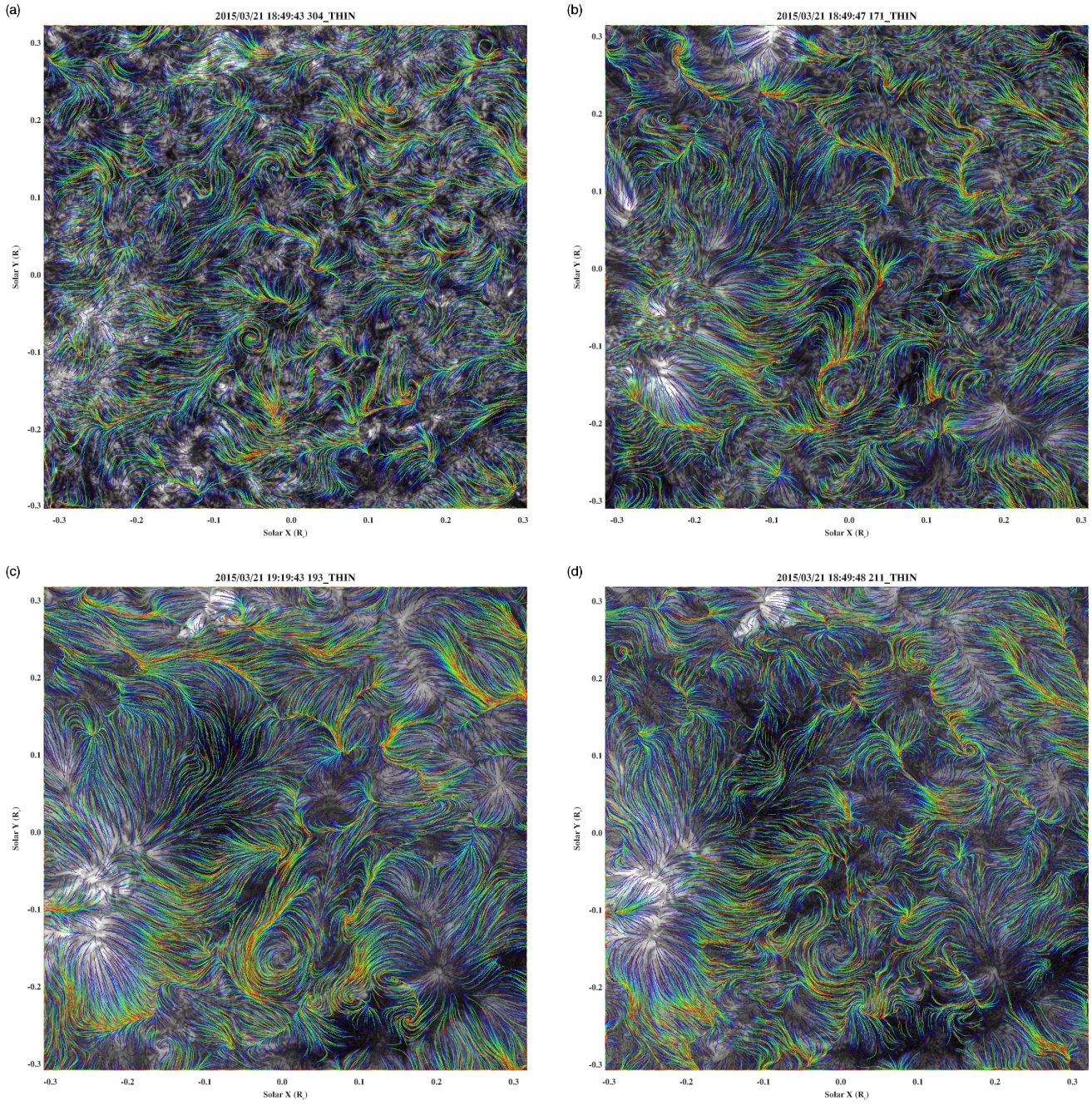

Figure 9. As figure 8 for the four AIA channels: (a) 304, (b) 171, (c) 193 and (d) 211Å.

In all channels, the vector field tends to converge from widely separated regions to narrow, elongated, spinal structures. In general, the direction of translation is outward from bright structures towards the narrow spinal structures. These tend to be aligned in narrow corridors that wind between the broad coherent regions. In the cool 304Å channel, the spinal structures extend to lengths of approximately 0.1Mm. In the hotter 193 and 211Å channels, they extend to 0.5Mm or more, with the 171Å channel at lengths in between. The vector fields as visualised in figure 9 are complex, intricate, and fairly stable over the 1-hour period.

The direct output of the LK method is a pixel (or sub-pixel) shift in the image plane. The dimension of each pixel can be expressed in km, and the cadence of the image sequence is known (12s). For the purpose of display and completeness, we present here velocity magnitudes in familiar units of km s^{-1}, but stress that these should not be interpreted as true velocities of features at the Sun. As will be discussed in the following section, the velocity magnitudes are sensitive to parameters of the time-normalization method and to other steps in the method. Furthermore, the derived 'velocities' are based on the projection of motions in the image plane (i.e. we have no information on the component towards or away from the observer). To avoid misinterpretation, we use the term 'optical velocity' as a specific label of the velocities arising from the LK method.

Figure 10 shows the magnitudes of the estimated optical velocities for the four AIA channels, averaged over the 1-hour period. In the 304Å channel, the average optical velocity is low ($\sim$16 km s^{-1} averaged over the whole region, maximum $\sim$28 km s^{-1}), with a complex distribution. In the 171Å channel, the mean velocity is also low (16 km s^{-1}, maximum 32 km s^{-1}), and the distribution showing some correlation with the underlying brightness structure. For example, the large region of high velocity in the bottom left of the image is aligned with the south-western flank of the bright active region. The 193Å channel has the highest average velocities (30 km s^{-1}, maximum 53 km s^{-1}), and also shows large-scale velocity structures correlated with the underlying brightness structure (bright structures tend to associate with higher velocities). There are broad regions of average/high velocities, separated by narrow channels of low velocities. Average velocities are lower for the 211Å channel (21 km s^{-1}, maximum 42 km s^{-1}). Velocity structure is also aligned with the brightness structures, but with smaller regions of average/high velocities surrounded by broad low-velocity regions.

The active region in the left of the image (centered at $x, y = -0.1, -0.25 R_{\odot}$) is interesting. In the 304Å channel, the optical velocity is lower than average in this region. The same is true for 171Å in the active region core, but with maximum velocities at the southern and western flanks. For 193Å, the core of the region has low velocity, whilst the southern flank has maximum velocities. For 211Å, in contrast to the other channels, the core does not show low velocity. To the northwest of the active region is a large dark region (as seen in the 193 and 211Å channels). This is a region of low velocities in the 193 and 211Å channels, yet shows average to high velocities in the two cooler channels.

The optical velocity distribution histograms are shown in the right column of figure 10. The three hotter channels show a broad peak with a small high-velocity tail, corresponding to small regions of high velocity at the periphery of bright active regions. This tail is not present in the 304Å channel. The results shown in this section are gained from means calculated from 300 observation pairs (every 12s) over a 1-hour period. The variation in estimated velocity over time will be discussed in a following section.

5. CHOICE OF PARAMETERS & VELOCITY UNCERTAINTY

The most important parameter in the time-normalization procedure is the width of the wide Gaussian kernel over which the temporal mean and variance are computed. Here, the processing and LK-method is applied with six different kernel widths to the central disk region in the 193Å channel. The kernel widths are 85, 127, 170, 212, 255, and 297s (standard deviation of the Gaussian kernel). The resulting translational vector fields are shown in figure 11. These results show that the choice of kernel width has only a small impact on the derived direction of the optical flows. The same large-scale structures are present, and similar, in all six fields. As we move from the 85 to the 170s

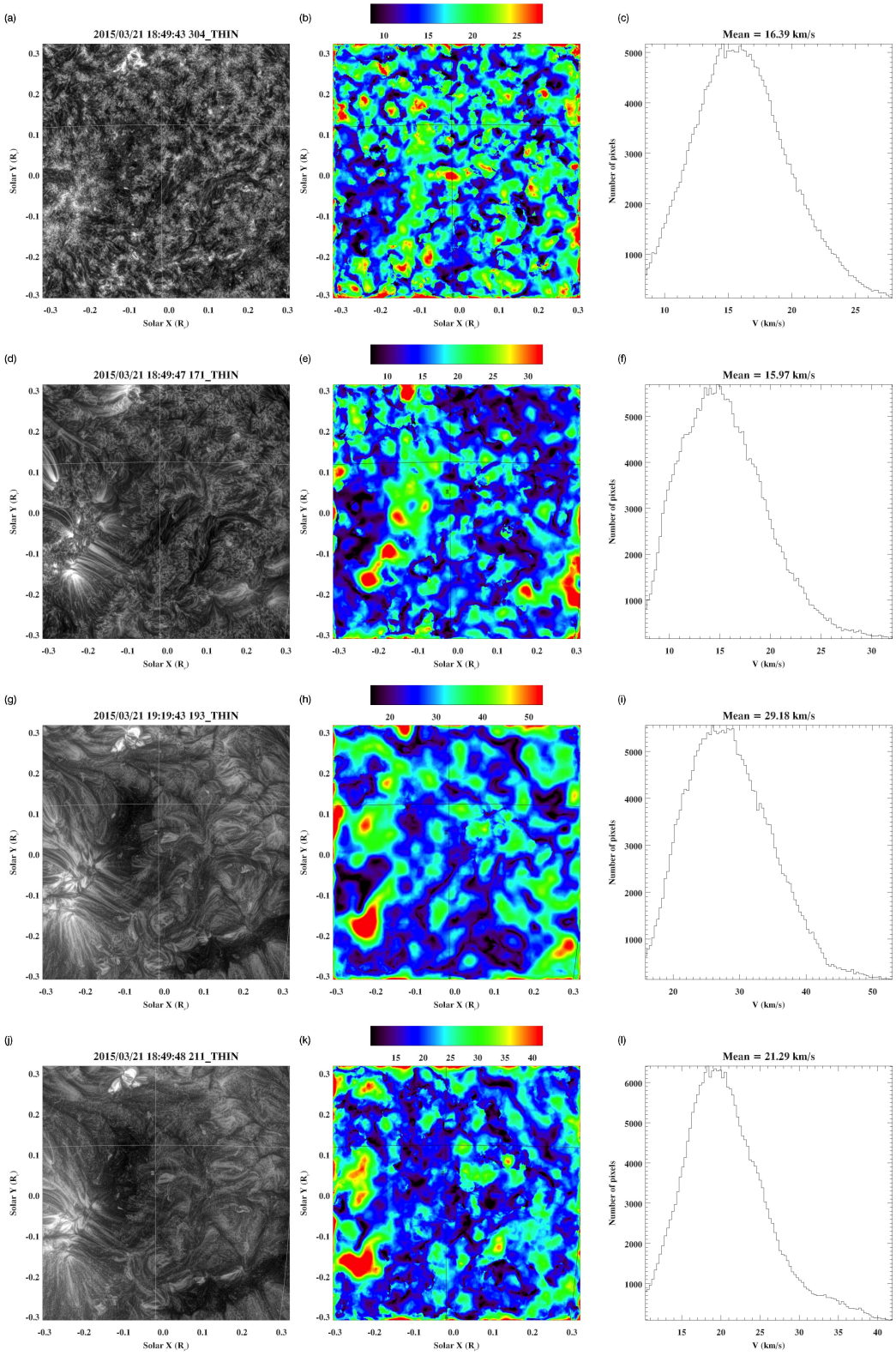

Figure 10. Left column: context images of the central disk region, in four AIA channels (top to bottom: 304, 171, 193 and 211Å). Middle column: maps of optical velocity magnitude. Note that the color scaling reference is different for each channel. Right column: optical velocity distributions for each channel.

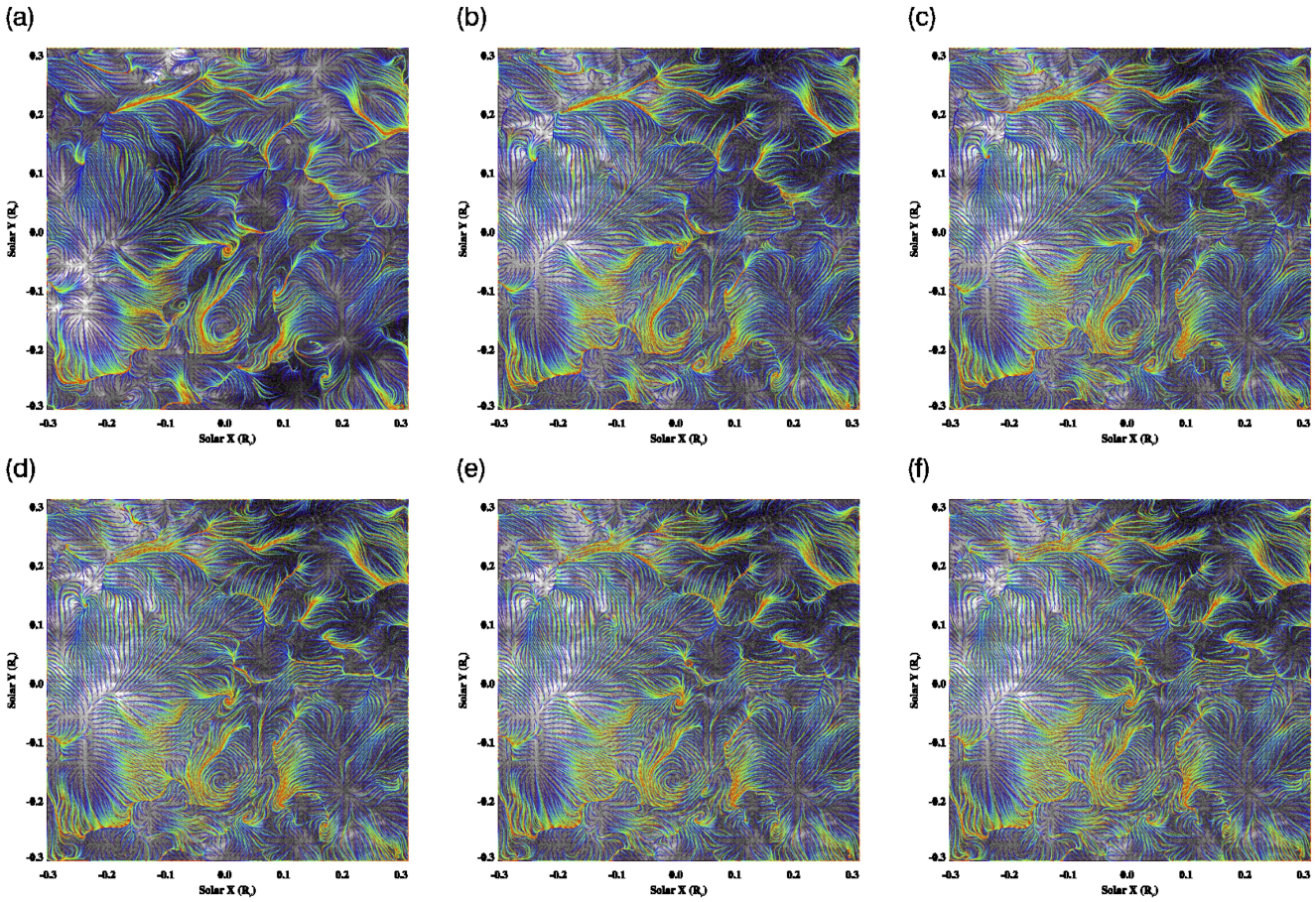

Figure 11. The translational vector field gained from applying the LK-method to time-normalized images in the AIA 193Å channel. Each panel show results arising from the use of Gaussian kernels of different widths during the time-normalization process, namely (a) 85, (b) 127, (c) 170, (d) 212, (e) 255 and (f) 297s respectively (standard deviations).

kernel, there are some differences at small scales. Between 170 and 297s, there is very little difference in structure.

Figure 12 shows the impact of different kernel widths on the optical velocity magnitudes. As with the vector fields, the *relative* velocity distributions look very similar. Yet the kernel widths have considerable effect on the magnitude values. At narrow kernel widths, derived velocities are highest. With increasing kernel widths, the velocities decrease consistently. This is shown as histograms in figure 13a. The mean optical velocity across the whole region drops from 35 to 20 km s^{-1} from the narrowest to widest kernel. Figure 13b shows that the decrease in mean velocity is less steep as we move between wider kernels. That is, the largest decrease is seen between the very narrowest kernel and the next widest ($\sim$5 km s^{-1} difference). The difference between the two widest kernels is only $\sim$1 km s^{-1}. The widths of the distributions (or the variance of the optical velocity across the region, shown as the error bars in figure 13b) also decreases with increasing kernel width.

The top row of figure 14 shows three selected paths through 193Å images, and the corresponding distance-time plots of intensity are shown in the middle row. Similar to figure 6, there is little evidence of coherent motion in these stack plots, and would normally not be considered for time-series analysis. The time-normalized stack plots are shown in the bottom row. The left column is a path traced along

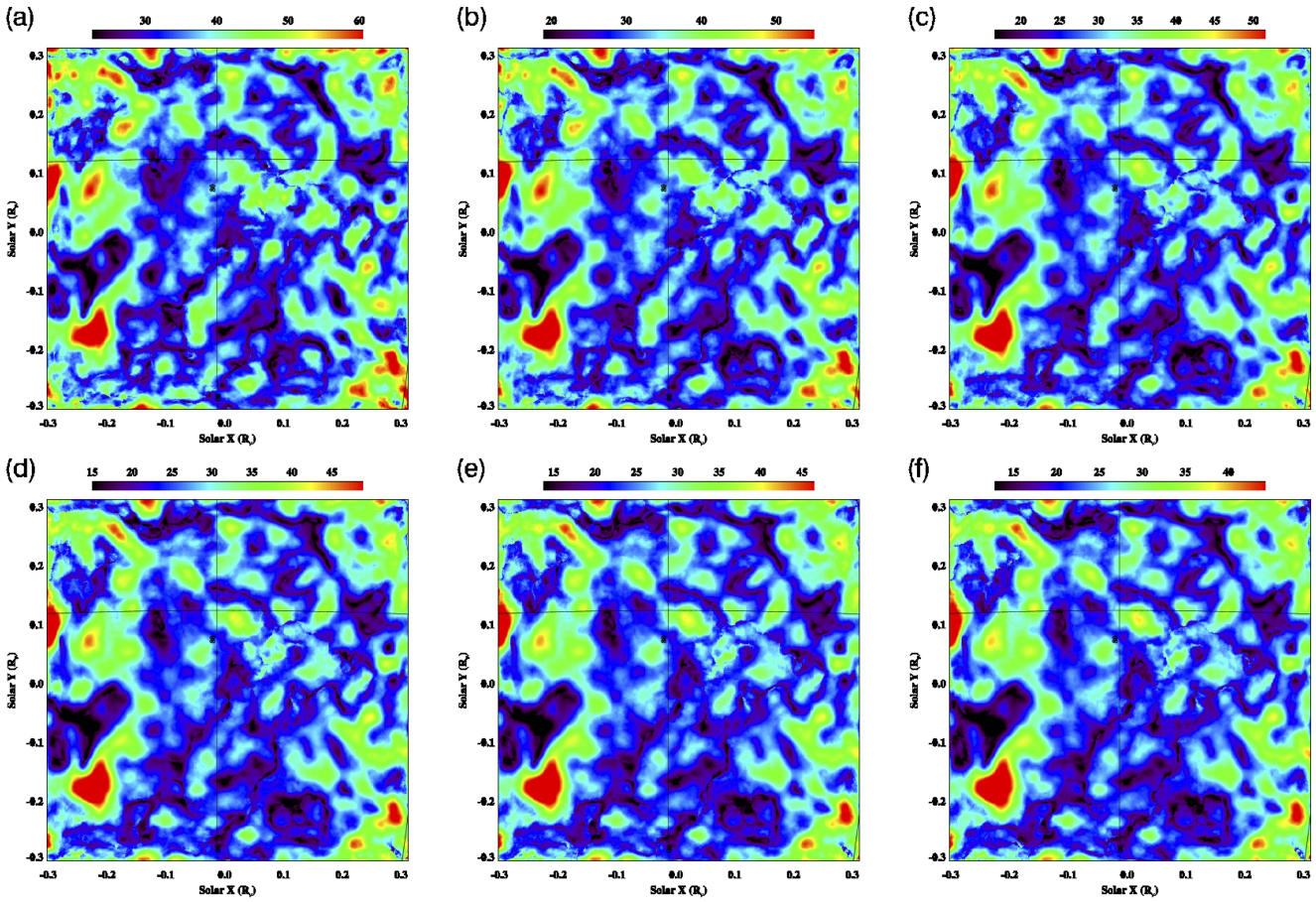

Figure 12. As figure 11, but showing the magnitude of the optical velocities.

a quiet Sun structure. The bottom stack plot (time normalized intensity) shows clear propagations along this path, and also shows that the optical velocities found using the LK-method (shown as red curves) match well with the gradient of these propagating disturbances. The optical velocities are fairly constant along the path and in time. The middle and right columns are for paths that begin near an active region. The time-normalized stack plots again show very clear signatures of propagating disturbances. The clearest motions are seen along the segment of the path nearest the active region (at the left side of the stack plot). Here, the optical velocity is highest. The segment of the path furthest from the active region (at the right of the stack plot) show a continuation of the disturbances, but with a fainter signature and slower velocity.

As well as the choice of wide kernel width during the time-normalization process, spatial and time smoothing during processing introduces another systematic scaling of the optical velocity magnitudes. This is always a concern in optical flow methods applied to remote sensing data (particularly where no independent verification is possible). As described above, a narrow Gaussian kernel is applied for temporal smoothing during the time normalization process. Without this temporal smoothing, the results are considerably deteriorated. The width of the kernel is determined through trial and error, and is minimized under the criteria of achieving the appearance of coherent motions in movies of processed data. Smoothing in the spatial dimension, or the reduction of high-frequency components, is achieved through multiresolution decomposition (as described in Appendix 1). This also aids

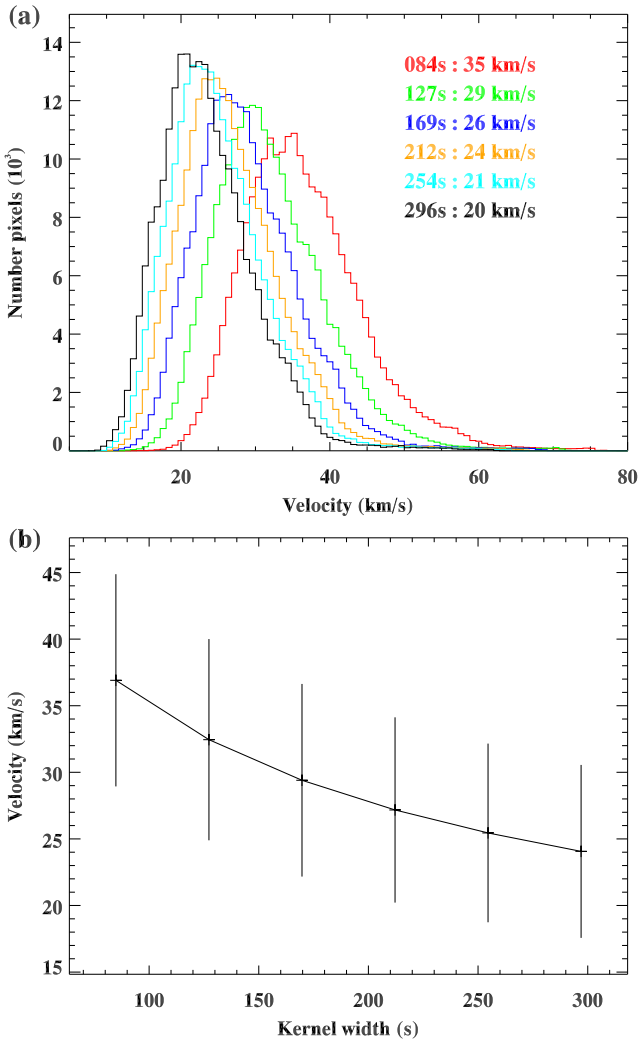

Figure 13. (a) Histograms of the optical velocity values across the central disk region for the 193Å channel, shown for the six different kernel widths as indicated by the colors. (b) The mean (line and crosses) and standard deviation (error bars) of optical velocity across the central disk region as a function of increasing kernel width.

in giving clean and coherent results. The core of the LK-method is based on applying equation 1 (Appendix 1). A glance at this equation shows that smoothing the data, in time or space, will directly influence the velocity estimates. Spatial smoothing will increase the estimated velocities (as the magnitude of the spatial derivatives is reduced), and temporal smoothing will decrease the estimated velocities. Furthermore, the finite spatial and temporal resolution of the observation will impose an inherent smoothing of any true motions in the corona, even without applying further smoothing during processing. Despite this systematic error, the stack plots of figure 14 show clearly that the LK method gives optical velocities that agree well with the propagation of disturbances along paths. Furthermore, the direction of the translational vector field is not influenced by smoothing (since the x and y directions are both smoothed equally) and is currently perhaps the most powerful potential application of the LK-method.

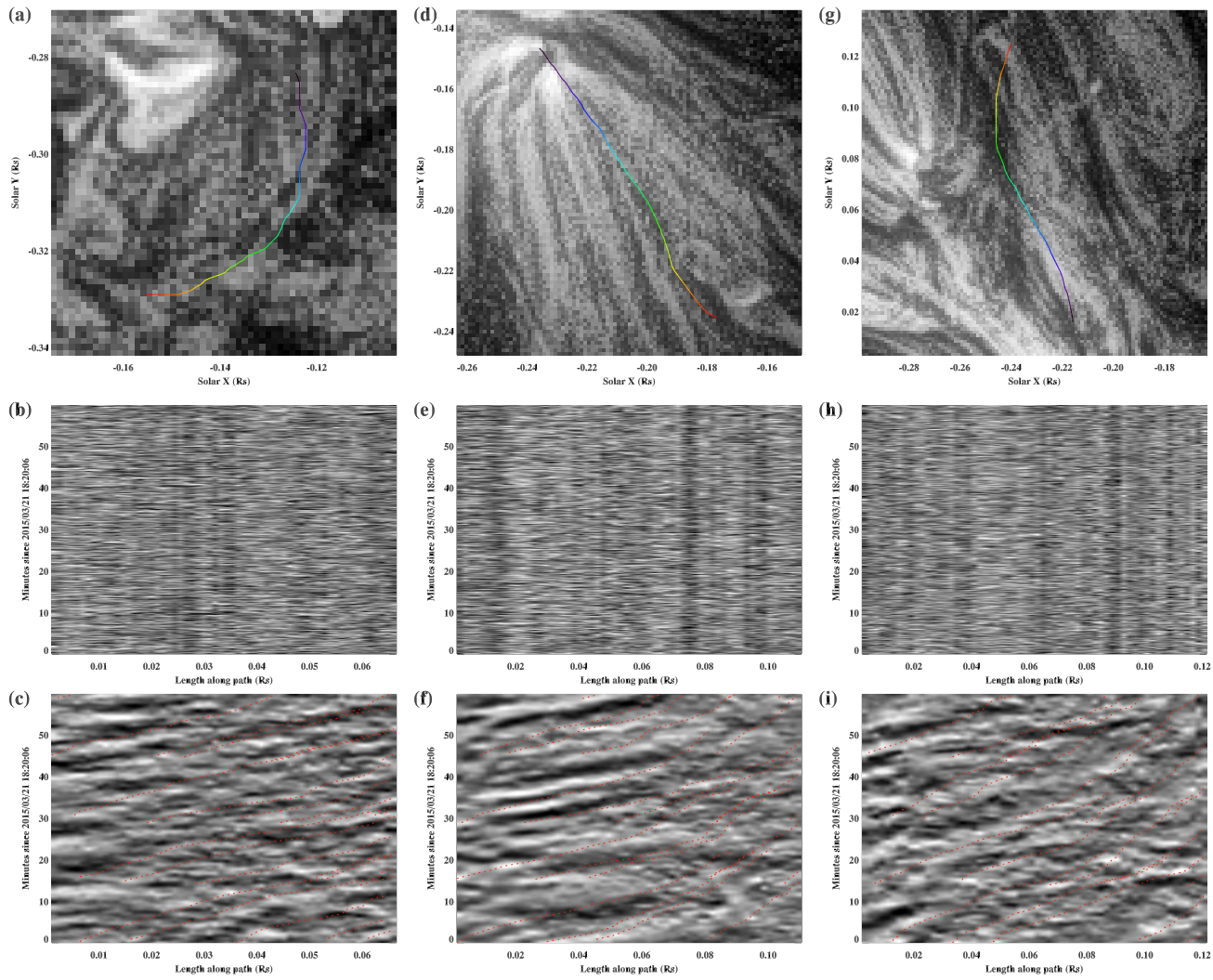

Figure 14. Top row: 193Å images of three selected subregions, overplotted with an isolated short path tracing the local velocity vector field. The color of the path indicates the direction of the translational vector (tracing from blue, green, yellow to red). Note the path is estimated from a translational field averaged over an hour's observation, whereas the background image is a snapshot at one time. Middle row: Distance-time stack plots showing the intensity of the original data along the path traced in the top row. Bottom row: Distance-time stack plots showing the time-normalized values along the path. The faint dotted red lines trace paths of motion given the optical velocity as estimated by the LK-method. Note the velocity is estimated specifically for the local region of the path and may change in time, so the red lines may vary in gradient along the path and in time.

In summary, the width of the wide kernel during image processing, and any spatial or temporal smoothing applied to the data, scales the estimated magnitudes of optical velocity. This scaling factor is the same in the image x and y directions, so that the orientation of the optical velocity field remains fairly constant when different parameters are tested. Our choice of an $150s$ kernel for our main results is therefore arbitrary, and the velocity scaling introduces a large uncertainty in the absolute magnitudes, but only a small uncertainty in relative velocities. This scaling and smoothing

Channel (Å)	$\bar{v_x}$	σ_x	$\bar{v_y}$	σ_y
304	3.08	4.32	0.19	4.28
171	2.96	6.05	-0.47	5.71
193	1.62	15.25	-0.60	11.47
211	2.21	9.12	0.08	6.53

Table 1. The mean and standard deviations of the velocity distributions shown in figure 15. All velocities are in km s^{-1}.

problem may only be solved with a future independent empirical constraint, beyond the scope of this paper. Such an independent measure of velocity would provide a calibration of the optical velocities and help realize the full potential of this method.

One promising idea for the calibration of the velocities is to exploit the solar rotation rate. Figure 15 compares the distribution of x and y components of velocities across the central disk region for the four channels, based on the main method parameters outlined in section 2. Fitting these distributions to Gaussians gives the means and standard deviations listed in table 1. The x velocity distributions in all channels are shifted to positive values, with means between 1.6 and 3.1 km s^{-1}. The y velocity distributions have means close to zero, with both negative and positive mean values. The systematic positive bias in the x velocities is due to the solar rotation. The photospheric rotation rate at the equator is close to 1.9 km s^{-1} (e.g. Howard et al. 1990), and the corona is expected to rotate at a similar rate to the photosphere at low latitudes (e.g. Morgan 2011). In principle, the systematic shift of x velocities to positive values may be used to calibrate the optical velocities. The problem arising from figure 15 lies in the different bias measured in each channel. Furthermore, from simple geometrical arguments, we would expect the magnitude of the x velocity bias due to rotation to decrease with increasing latitude (simply due to each pixel spanning a greater range of longitudes, not due to differential rotation). This calibration requires the study of a large set of data at a range of latitudes. We are in the process of analysing datasets observed at several periods over a whole solar rotation, and will use the results to calibrate the velocity distributions. From figure 15, the positive x-velocity biases are reasonably close to the velocity due to rotation, so are not unreasonably far from true velocities at the Sun. Note that *relative* errors are small, and that the directions of the velocity vectors are reliable. Despite this, the velocity magnitudes given in this paper should not be interpreted as the true speed of disturbances in the corona - the uncertainties are large.

6. VARIATION IN TIME

Given that the direction of the velocity vectors seem insensitive to choices of processing parameters such as smoothing, then the variation in the estimated velocity direction over time is a convenient measure of uncertainty. Figure 16 quantifies the uncertainties in the results of the LK method as applied to data. This variation over time is shown for the 193Å channel in figure 16a. The variation of the velocity magnitude over time (relative to the mean magnitude) is shown in figure 16b. Both show a similar distribution. Regions of high variation are distributed along narrow ridges. These are closely associated with regions of low velocity (see figure 10h), and the narrow elongated regions where the velocity vectors seem to converge (see figure 9c).

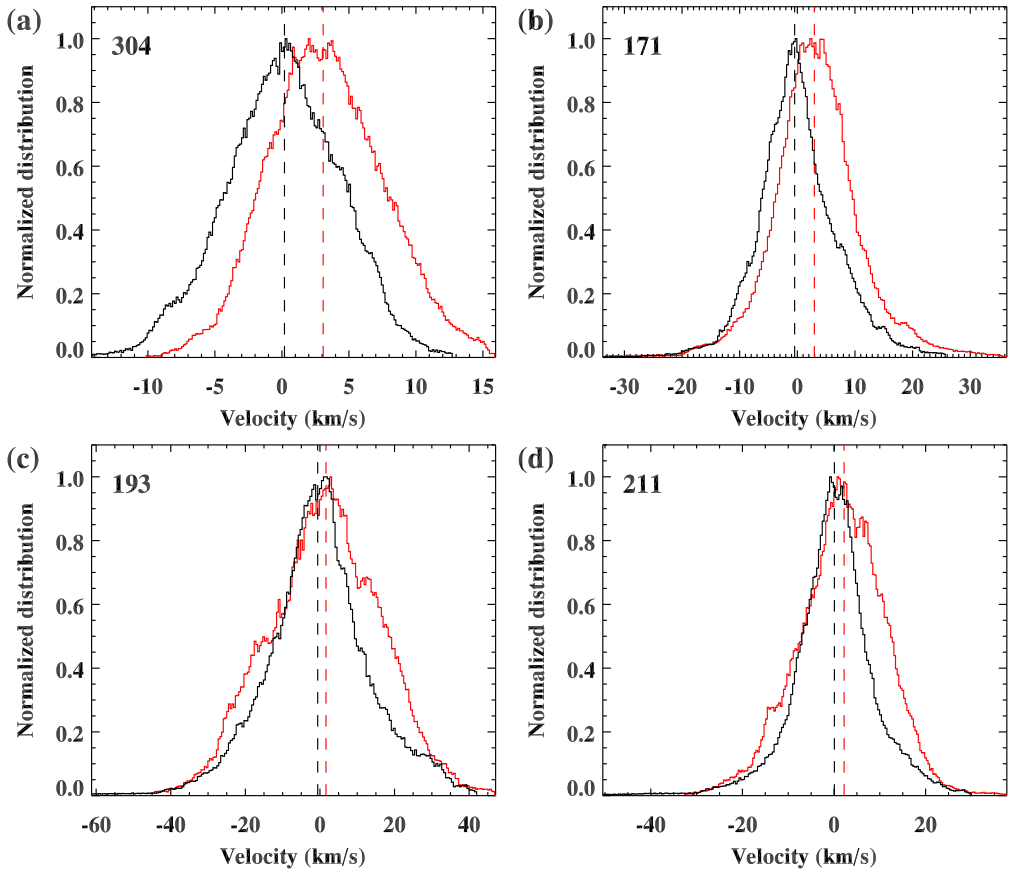

Figure 15. Histograms of y-velocity (black) and x-velocity (red) components for the (a) 304, (b) 171, (c) 193 and (d) 211Å channels for the central disk region. The vertical dashed lines show the mean determined by fitting each distribution to a Gaussian function.

The black cross in figure 16a indicates the pixel where the largest angular variation is measured in the 193Å channel. This is a position where we would expect to see the most noise in the results. Figure 16c shows the direction of the velocity vector at this pixel over a time period of an hour. Clearly the large variation at this pixel is not solely due to noise. Over time, the velocity vector can occasionally make large erratic jumps in direction. However, between most time steps, the change in direction is small and follows a smooth longer-term rotation over the hour. Figure 16d shows the velocity magnitude at this pixel over time. Again, this value is varying smoothly at timescales of a few minutes, rather at the observational and procedural timescale of 12s (i.e. the time between pairs of images used as input for the LK method).

Figure 17 shows the velocity time series for the 193, 171, 211 and 304Å channels at the pixel of smallest directional variance in the 193Å channel, indicated by the white triangle in figure 16a. Figure 17a shows that the direction of the velocity vector in the two hotter channels varies very little over the hour, and the motion is strongly aligned with the magnetic field structure. The 171Å direction varies considerably more, although the changes are smooth, and show variation over timescales of several minutes. The 304Å channel shows large directional changes, but again the changes are smooth and vary over timescales of several minutes, except for the occasional abrupt jump (note that several of these apparent jumps are caused by the display range of $\pm 180°$). Figure 17b compares the

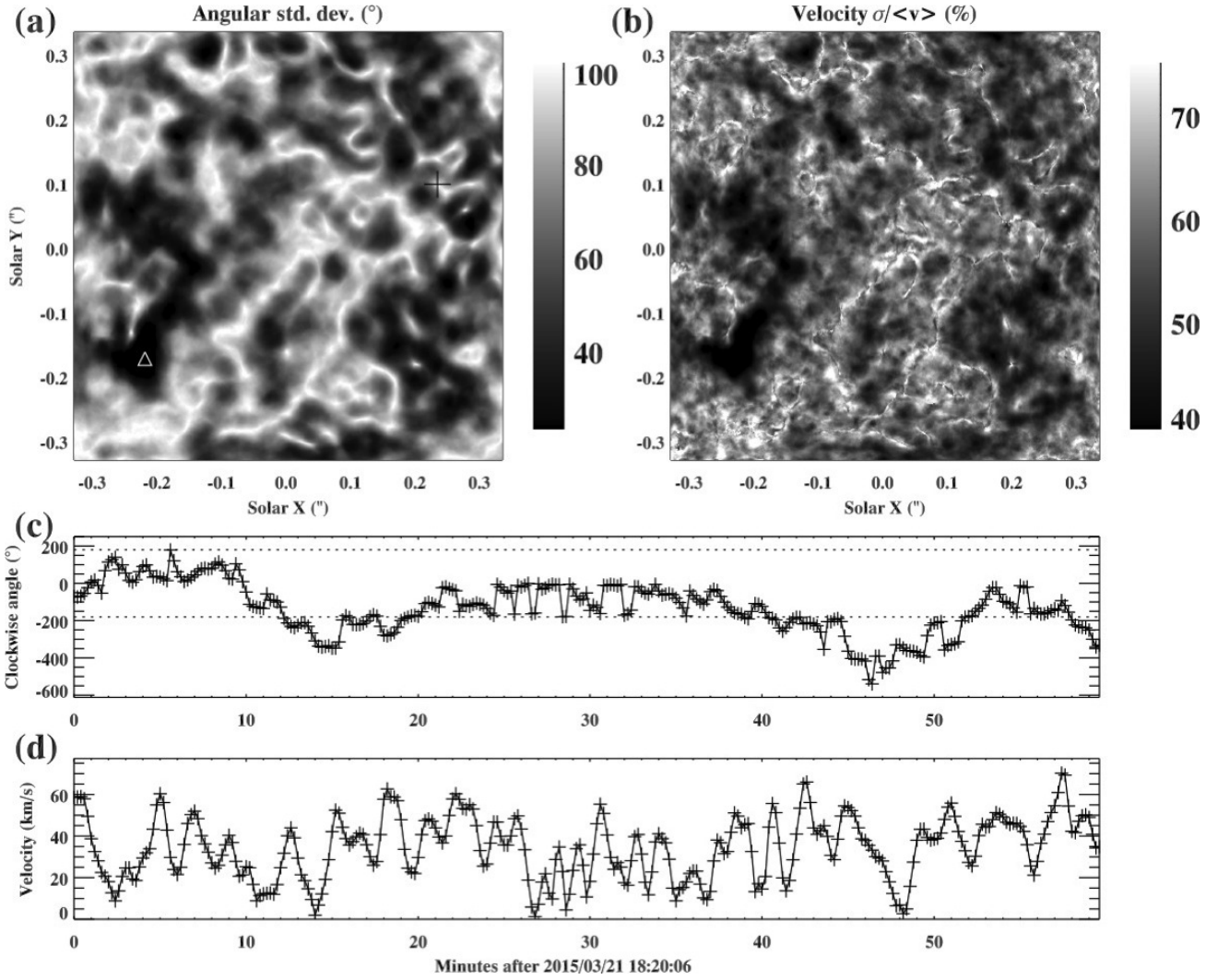

Figure 16. (a) The standard deviation over time of the direction of the 193Å channel velocity vector, in degrees as represented by the color bar. The standard deviation is measured from the local median direction at each pixel. The black cross is the pixel with the highest variation of direction. The white triangle shows the pixel with the lowest variation in the direction. (b) The standard deviation of the 193Å channel velocity magnitude over time, as a proportion of the mean magnitude. (c) The direction of the velocity vector as a function of time at a pixel of interest (indicated by the black cross in panel (a)). Note that the y-axis scale wraps beyond the $\pm 180°$. The dotted horizontal lines show the $\pm 180°$ boundary. (d) The velocity magnitude as a function of time at the pixel of interest.

velocity magnitudes for all channels. The variation is smooth and varies over minutes rather than the observational cadence of 12s. In magnitude and direction, there seems to be no strong correlation between channels, although the dominant (or mean) direction is similar for all. The only significant correlation is between the 193 and 211 channels, with above 40% correlation between the channels, in both magnitude and direction.

An important question is whether there are significant periodicities in the velocity magnitudes. Figures 16c-f show wavelet power spectra for the velocity magnitude for each channel. The 193Å spectra are dominated by 8 minute periodicities. The 171Å total velocity has a clear band of sig-

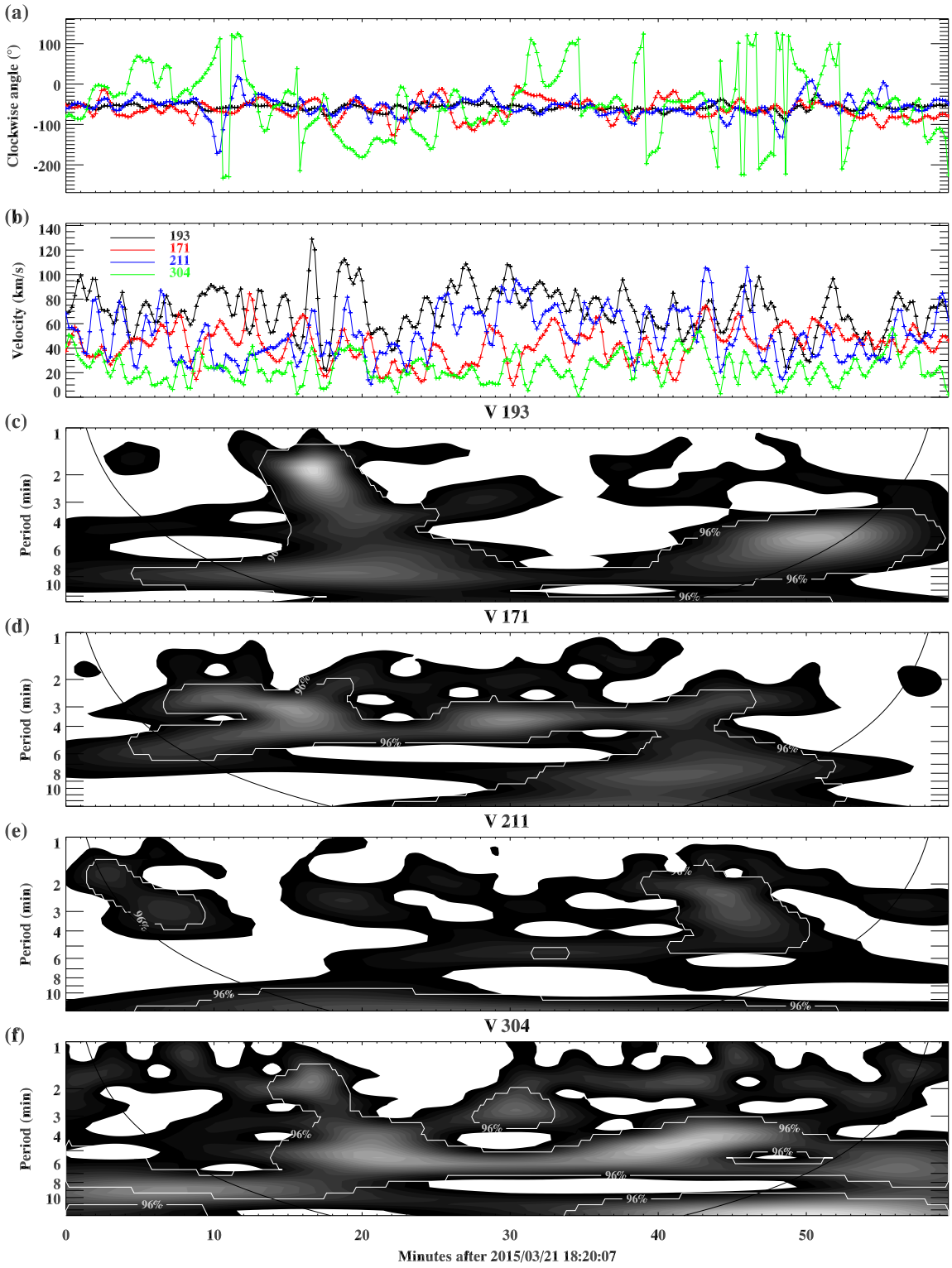

Figure 17. For the pixel of smallest directional variance, indicated by the white triangle in figure 16a, these plots show: (a) the angle of the velocity vector and (b) the velocity magnitude for the 193Å (black), 171Å (red), 211Å (blue) and 304Å (green) channels. (c)-(f) wavelet power spectra for the 193, 171, 211 and 304Å total velocity magnitudes respectively. Areas of significance (bounded by white contours) are determined using the procedure of Appendix 2.

nificant oscillation at a periodicity of 3-5 minutes, lasting for around 40 minutes. The 304 channel has a similar clear band at a longer periodicity of 4-8 minutes. However, there is considerable uncertainty in these periodicities introduced by (i) the time window of the time-normalization process and (ii) further steps in preparing for the Lucas-Kanade method (spatial smoothing). Quantifying these uncertainties is a large task beyond the scope of this paper. We are currently looking in detail at time series analysis of intensities and velocities, and the relationship between them. Critical to this study is how time-normalization affects the results. Figure 18a shows an intensity time series for the 193Å channel near the active region. This series has a peak in periodicity at 10m, as shown in the global power spectrum of figure 18b. Figure 18c shows the time-normalization transformation of the signal for several different choices of the wide Gaussian kernel width. The resulting power spectra are shown in figure 18d. The main effect of the time normalization is to reduce the relative power at long and very short periods, so that the relative power in the periodicity range between the width of the narrow kernel and the wide is increased. In particular the relative strength of the small peak near 4 minutes is greatly increased. The main 10 minute peak is shifted to 11 minutes. For a narrow choice of wide Gaussian kernel (red line), the 4 minute peak is strong and the 11 minute peak is weak. As the width is increased, the 11 minute peak becomes dominant. The time normalization is similar to a bandpass filter, except with the additional step of normalizing by the local amplitude, thus its effect on power spectra is difficult to interpret. Even more difficult to interpret is time series of velocity magnitudes, compounded by the additional step of the LK method. A velocity time series is shown in figure 18e, with the power spectrum shown in 18f. Our results seem to show significant periodicities, but we have no further comment without a better understanding of the impact of the processing on the results. This will be addressed by a better analytical understanding of the behavior of time-normalization filtering, and through a brute force approach where many test signals are fed into the process, in order to test different parameters; the subject of a future study.

7. DISCUSSION

The most important question is what are these universal disturbances revealed by time normalization. They are present everywhere at all times, in all the four channels presented in the results. They are so faint that they are not visible without appropriate processing. Figure 19 shows that the disturbances, in most regions, typically have an amplitude of at most ∼4 DN/s, or less than 2% of the background signal. Only small isolated regions, typically near active regions, have amplitudes above ∼10 DN/s. These regions also have a higher disturbance velocity. Previous studies of dynamic events in EUV images generally show events (oscillations, or propagating disturbances) of higher signal, that are directly observable in the AIA images or in time-distance plots, or are present as significant periodicities in time series analysis.

Figure 20, and the accompanying movie, show detail of the vortex structure circled in green in figure 5. The left panel shows a simple MGN image of this region. The EUV structure is quite clearly a set of nested circular profiles around a central region. The middle panel shows the corresponding time-normalized image. The accompanying movie clearly shows anti-clockwise rotational motions around the center. The right panel shows how the velocity field follows this rotational motion in the correct central region. Towards the edges of the displayed region, outside the vortex, the field lines still follow the underlying features seen in the EUV images. As shown in figure 9, the velocity field throughout the central disk region closely follows underlying structure seen in EUV images. This qualitative comparison strongly suggests that the tracked motions are field-aligned.

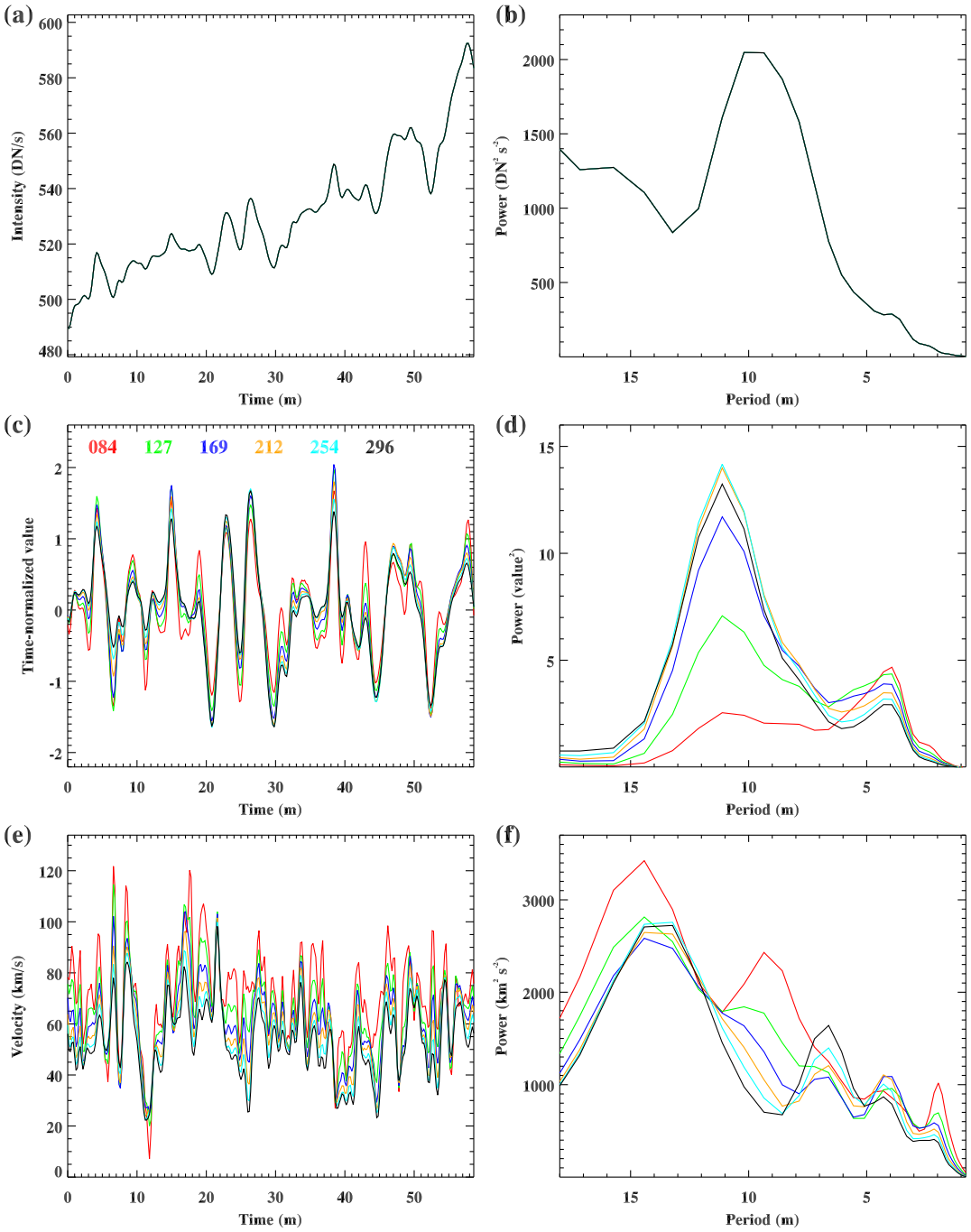

Figure 18. (a) The 193Å intensity over an hour at a pixel near the active region. (b) The resulting global power spectrum as gained from taking the mean of a wavelet power spectrum over time (similar to a Fourier power spectrum). (c) The time-normalized values at this pixel for several time window widths indicated by the color labels (in seconds). (d) The resulting global power spectra. (e) The velocity magnitude time series arising from the LK method at this pixel and (f) the power spectra for the velocity magnitude.

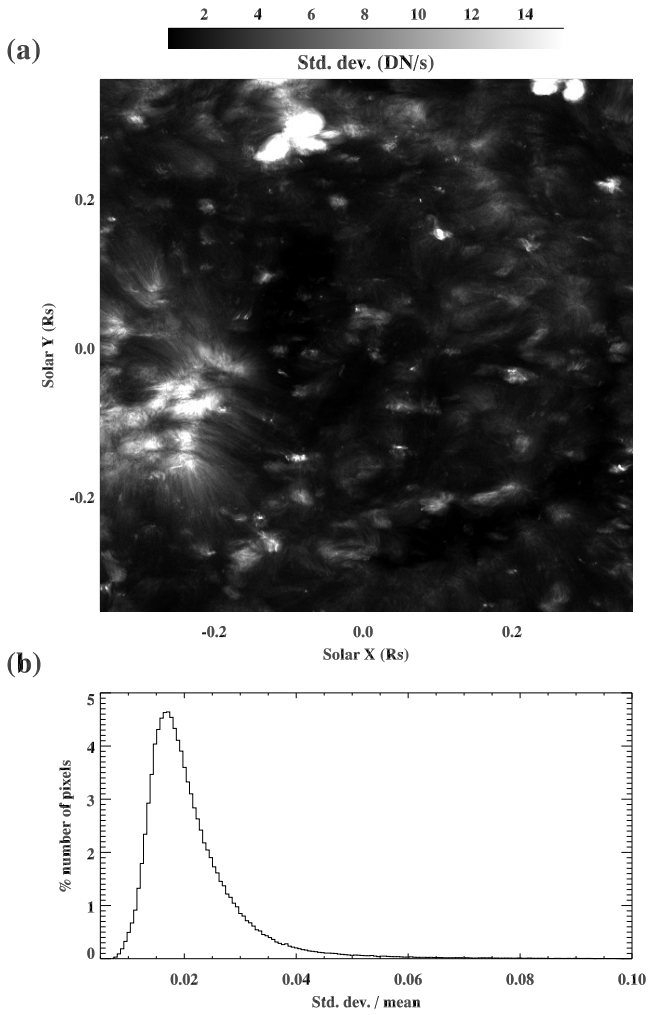

Figure 19. (a) The standard deviation of values (in DN/s) measured within the 15 minute Gaussian-weighted time window for the 193Å channel. This is a measure of the amplitude of the measured disturbances plus noise. The standard deviation shown here is the mean deviation over two hours of observation. (b) Histogram of the standard deviation relative to the mean signal at each pixel throughout the region depicted in (a).

Regions of the velocity field which show the lowest velocity magnitudes (see figure 10) are aligned with the narrow elongated convergence regions seen in the vector field of figure 9, and with the regions showing the highest temporal variation in velocity direction and magnitude (as shown in figure 16). These regions are interpreted as regions dominated by vertical flows along largely vertical field which is aligned with the line of sight, which cannot be visualised or estimated by image processing and the LK-method. The component of velocity in the image plane is small, and is subject to the largest variations in direction and velocity magnitude. A thorough quantitative comparison of the velocity fields with magnetic field models will be attempted in future studies. The motion tracking results show potential as a new constraint on magnetic field models, or at least provide a measure of their accuracy. For example, magnetic field extrapolations of the vortex region of figure 20 show a field extending radially outwards from the center of the vortex, contrary to the observed circular structure seen in EUV images and the rotational motion revealed by time normalization and the motion tracking

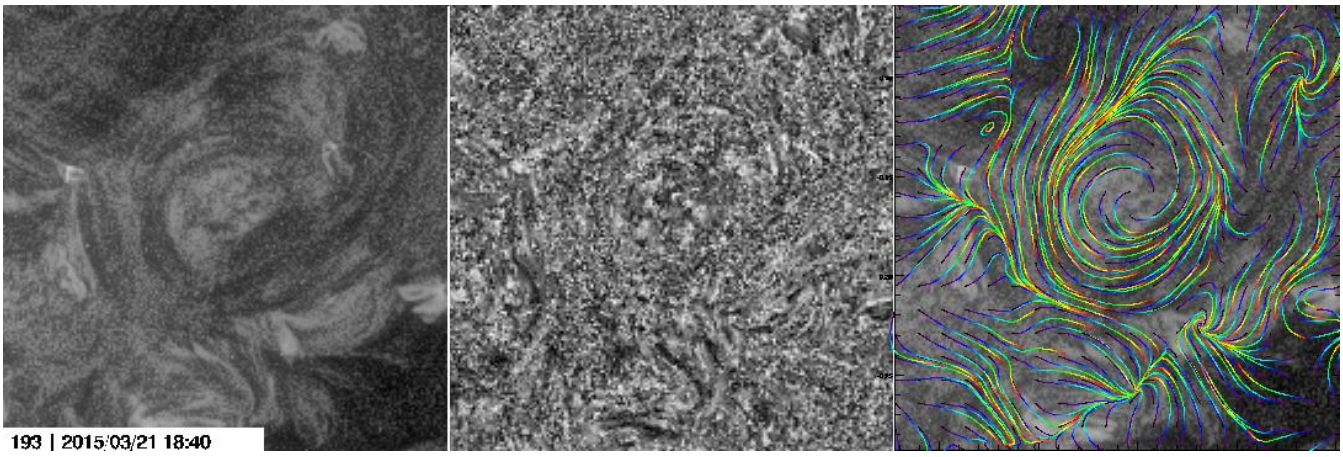

Figure 20. Left panel: MGN image showing detail of the vortex region centered on $x, y = 0.0, -0.15$ (see, for example, the green circled region in figure 5), as seen in the 193Å channel. Middle panel: time-normalized image of the same region. Right panel: velocity field lines overplotted on the MGN image. It is important to view the accompanying movie to visualise the rotational motions in this region.

velocity field. Thus, in certain regions, the velocity vector field gives a more correct mapping of the underlying magnetic field structure than that gained from photospheric field extrapolations, at least in the 2D image plane.

Figure 21a shows a short path traced by the velocity vector field of the 193Å channel. A wavelet analysis of the time-normalized intensities along the path leads to the global power spectra shown in figure 21b, displayed as a function of distance along the path, and periodicity. Oscillations in intensity are dominated by ∼11-minute periodicities nearest the active region, with a weaker component near 5 to 6 minutes. The periodicities decrease with increasing distances along the path, and are dominated by 4 to 8 minute periodicities towards the end most distant from the active region. Note that these periodicities are subject to the caveats raised in the preceding section - the time normalization has a bandpass filter effect, and introduces a shift in the main power spectra peaks.

The components of velocity parallel and perpendicular to this path is plotted in figures 21c and d respectively, as a function of distance along the path, and of time. The parallel component shows intermittent pulses of high velocity moving out from the nearby active region. These pulses continue out along the path and experience deceleration. The perpendicular component (figure 21d) is more complex. There are short periods of perpendicular velocity to both directions, with the direction changing over timescales of a few minutes. The perpendicular velocity is generally limited to magnitudes below 10 km s^{-1}, with only very short periods where the velocity magnitude is above 20 or 30 km s^{-1}. Figure 21e shows the cumulative perpendicular displacement over the hour as calculated from the perpendicular velocity. Typical displacement is on the order of hundreds or a few thousand km, over tens of minutes. The cumulative perpendicular displacement over an hour shows a consistent drift of the plasma towards one perpendicular direction at the path center, and to the other direction at both ends of the path. This is due to slow, large-scale motions including solar rotation and general movement of structures near the active region. Even at the maximum perpendicular velocities, around 10 consecutive AIA observations are needed to register a single pixel shift in the position of the underlying magnetic structure. The width of the structures (i.e. loops), as observed on the disk, are considerably wider than one pixel. It is possible therefore that the motions revealed

by time normalization are a plasma response to perpendicular oscillations in the coronal magnetic field - oscillations that would be very difficult to detect directly in the movement of structures in AIA images.

Summarizing the results: the disturbances are faint, ubiquitous and continuous (in the sense that they continuously appear everywhere). They are field-aligned and may contain some significant oscillations with periods of minutes, or repeat quasi-periodically at a timescale of minutes. Velocities are lower in the cooler channels. The structure seen in the velocity field is smaller-scale and less coherent in the cooler channels, probably reflecting the structure of the magnetic field with height in the corona. Velocities show directions and magnitudes that change smoothly in time, over timescales of minutes. Regions of low mean velocity/high time variance show slow rotations of the motion direction, over timescales of several tens of minutes. Regions of higher mean velocity/low time variance show a more constant direction over time, with large variation seen only in the 304Å channel.

There are two aspects to these results that demand interpretation: (1) The nature of the coronal disturbances themselves and (2) their cause, or driver. As mentioned, their nature could be the plasma response to intermittent packets of propagating perpendicular disturbances in the coronal magnetic field, or magnetic waves. Their driver must be a phenomenon that is ubiquitous in the low solar atmosphere, transmitted as disturbances in the overlying corona.

Time-distance plots of wavelet-enhanced EUV images have shown faint propagating disturbances in several coronal regions (Stenborg et al. 2011). Based on their results, they claim that the disturbances are a 'coronal phenomenon that exists permanently everywhere'. Their study, focusing on a quiet-Sun anemone-like structure and an active region, show mean propagation velocities of around 60-90 km s^{-1}, with amplitudes of 2 to 5% of the background intensity. The propagations revealed by their study, and by Wang, Ofman, & Davila (2009) for fan-like loop structures, are certainly the same as revealed by time normalization. Stenborg et al. (2011) found significant oscillations (following high-pass filtering) at ∼8 minutes, and multiples of 8 minutes, although their input cadence was limited to ∼2.5 minutes. Wang, Ofman, & Davila (2009) found both 14 and 26 minute oscillations in the propagating disturbances. Both studies give a likely interpretation of slow magneto-acoustic waves, with Stenborg et al. (2011) placing emphasis on propagation along open field, although our study shows that the disturbances exist in all coronal structures (open or closed).

Faint propagating disturbances seen in cellular plume structures by Sheeley et al. (2014) show ∼100 km s^{-1} speeds, and 5-8 minute repetition time. Their emphasis is less on periodic oscillations, and on a repetitive series of elongated ejections emanating from unipolar magnetic flux concentrations, with uncorrelated phase at adjacent regions. They do not find a continuous flow, and give a picture of the phenomenon as a system of independent conveyors of plasma parcels along the magnetic field. Mandal et al. (2015) show quasi-periodic propagating disturbances in an active region fan loop system, with oscillations of 3-10 minutes. They find velocities of $17 - 60 \pm 7$ km s^{-1} for the 171Å line, and $37 - 87 \pm 11$ km s^{-1} for 193Å, and use this temperature-dependent propagation speed as support for slow magnetoacoustic waves. The same is true for our findings: different channels exhibit different speed distributions, and this may be support for a slow-mode wave interpretation.

There is no doubt that previous studies of faint propagating disturbances (e.g. Stenborg et al. 2011; Wang, Ofman, & Davila 2009; Sheeley et al. 2014; Mandal et al. 2015) are based on the same phenomenon as revealed by time normalization. We find very similar results for the fan-like system of loops near the small active region - indeed, the strongest, most obvious, and highest-speed

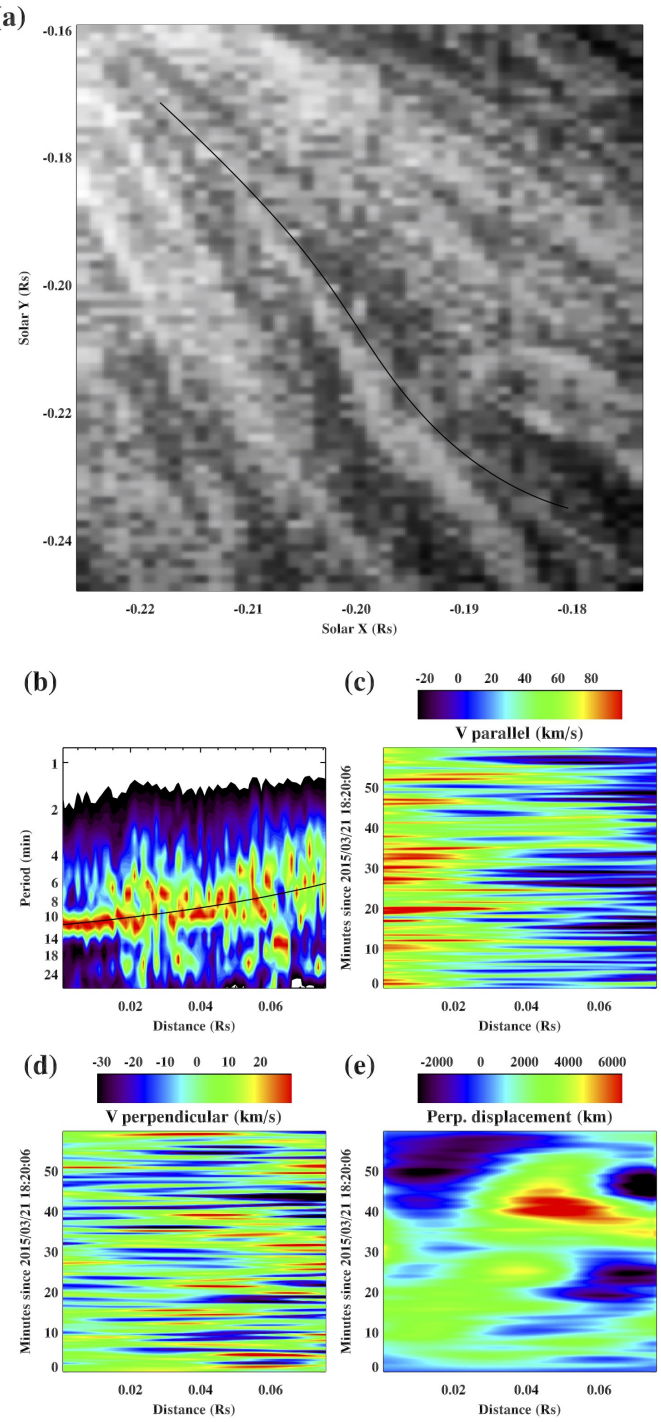

Figure 21. (a) 193Å image of a region of interest, with a path tracing the local velocity field shown in black. The start of the path (in the top left corner) begins at the pixel of minimum variance shown as a triangle in figure 16a. (b) Global power spectra of the time-normalized intensity as a function of distance along the path, and of periodicities in minutes. The black line shows a fit to the power spectra as a function of distance along the path. (c) The parallel velocity component along the path as a function of time. (d) The perpendicular velocity component. (e) The cumulative perpendicular displacement across the path as calculated from the perpendicular velocity.

disturbances are measured in this region, and most previous studies have concentrated on similar regions. Yet faint disturbances are present everywhere, in all regions. The mean velocities we find are lower than those found using distance-time plots in previous studies (although our approach needs further calibration). However, over the hour dataset presented here, our highest velocities are entirely consistent with previous studies. Thus the brightest disturbances are propagating at higher velocites, and these are the ones reported in previous studies. In the periods between, or in the absence, of these brighter propagations we measure a lower field-aligned velocity, therefore there must still be a very faint time-varying motion along the magnetic field. Time-distance plots are dominated by the path of the brighter disturbances, and the fainter motion may not be visible. This suggests that there may be a large range of brightnesses, speed and size to the disturbances, with the fainter disturbances possessing a lower speed.

Establishing the nature of the disturbances still leaves open the question of their source, or driver. Since spicules are ubiquitous in the transition region/low corona, they have for a long time been a prime candidate for transporting energy to the corona, and maintaining high temperatures (Raouafi et al. 2016; Tsiropoula et al. 2012; Sterling 2000). Certainly many of the results presented here for the low corona share similarity with observational studies of spicules. Intensity oscillations in spicules indicate a photospheric driver and are typically of a few minutes (e.g. Zaqarashvili & Erdélyi 2009). Wave phase speeds in spicules are estimated to be in the range of a few tens to 200 km s^{-1} (De Pontieu et al. 2007). De Pontieu et al. (2017) show direct causal connection between a spicule observed in the transition region and subsequent coronal disturbances as observed by AIA in the 171 and 193Å channels. Their study, supported by an advanced 2.5D magnetohydrodynamic simulation, shows that propagating coronal disturbances may be caused by a complex sequence of phenomena, including flows, shock waves, magnetic waves and plasma heating through current dissipation. To further complicate the picture, they show that new coronal loop strands may be created by spicules, which may appear as propagating disturbances in time-differenced images.

The modelling work of De Moortel et al. (2015) shows the difficulty of distinguishing waves from flows given current observations. What time normalization, and the LK method gives is the chance to characterize the disturbances over large regions and over long time periods. This may help to distinguish the nature of the disturbances, based on propagation velocities at different temperature regimes in different regions, and on a detailed search for significant oscillations and phase correlations between regions and different temperature channels. A future study of a larger dataset may, through statistical and direct causal approaches, and comparison with other data from the lower atmosphere, give insight into the source of the propagating disturbances. We can only say that their source must be ubiquitous at the coronal base (as are spicules), and should share some common characteristics with the coronal disturbances (e.g. periodicities/repetition timescales and possibly velocities). Ireland et al. (2015) show that coronal power spectra are best fitted by a power law plus a Gaussian peak in power at certain periodicities, suggesting a superposition of many events along the line of sight, consistent with a heating mechanism that operates everywhere by small events. Certainly our results are consistent with this interpretation.

8. CONCLUSIONS

This work presents a new image processing method that reveals motions in high-resolution EUV images of the corona. The motions are propagating enhancements which are very faint - typically 2% of the background intensity, on the order of 2-10 DN/s (i.e. the signal normalized by the exposure

time). The motions are seen at all times everywhere on the solar disk and in many off-limb regions. An adapted Lucas-Kanade method is applied to the processed images, enabling detailed tracking and characterization of the motions. In this paper, a full hours' worth of data is processed in four AIA channels. Averaged over the hour, the motions are seen to trace the underlying large-scale magnetic field. The intricate motion vector field describes large-scale linear (or coherent) regions, narrow corridors of converging vectors, and large vortices. Comparison with the structure seen in EUV images and an analysis of the time variation of the velocity field suggests that the narrow corridors of converging vectors are associated with regions where the magnetic field is largely vertical (at least at the low heights where the EUV emission is strongest). The large regions of linear vector fields are associated with large-scale low-lying closed field or loops. Indeed, the motion vector field traces very closely the underlying structure seen in the original intensity images. The velocity field is structured at smaller scales in the cooler channels, whilst the hotter channels are coherent over larger scales, reflecting the decreasing complexity of the magnetic topology with increasing coronal height, and the increasing size of coronal loops with height. The magnitudes of the detected velocities, when averaged over long periods, are on the order of few tens of km s^{-1}. Time series of velocities reveal smoothly-changing direction and magnitudes, varying smoothly on the order of several minutes. The magnitude of velocities perpendicular to the mean direction of the underlying magnetic field are sub-pixel movements at the AIA image cadence, and therefore impossible to observe directly as movement of structures (e.g. loops) in the unprocessed AIA images, particularly considering that the width of these structures can span several pixels. The propagating disturbances are likely slow-mode waves, consistent with previous observational studies. Their behavior suggest a close link with photospheric drivers and their source must also be ubiquitous and continuous at the coronal base.

The method leads to a rich new source of information on a coronal phenomenon which has hitherto remained largely hidden (with the exception of brighter, more obvious, motions and disturbances in isolated regions or events). There are exciting possibilities for tracking motions in several AIA channels simultaneously (dominated by different height layers in the corona), plus the potential for combining this with other instruments (e.g. application to IRIS slitjaw images, plus spectral Doppler shift and broadening information from spectrometers), thus extending the study to transition region/chromospheric layers. Furthermore, the velocity fields seem to give an intricate mapping of the underlying magnetic field. This must be verified through comparison with models and other data, and a more comprehensive comparison between EUV images and the resulting velocity fields. Any observational constraints or verification on coronal magnetic field models will be an important advancement, and this new method will in future provide such a constraint.

We thank Dr. Youra Taroyan and Dr. Xing Li at Aberystwyth University, and Prof. Miloslav Druckmüller at Brno University of Technology, Czech Republic for useful discussions on this work. Huw Morgan conducted part of this work under a Leverhulme award. Joe Hutton is supported by an STFC grant to Aberystwyth University. The AIA/SDO data used here is courtesy of NASA/SDO and the AIA science team.

REFERENCES

Antolin, P., Shibata, K., & Vissers, G. 2010, ApJ, 716, 154

Aschwanden, M. J., Reardon, K., & Jess, D. B. 2016, ApJ, 826, 61

Aschwanden, M. J., Winebarger, A., Tsiklauri, D., & Peter, H. 2007, ApJ, 659, 1673
Asensio Ramos, A., Requerey, I. S., & Vitas, N. 2017, A&A, 604, A11
Bradshaw, S. J., & Klimchuk, J. A. 2015, ApJ, 811, 129
Bryans, P., McIntosh, S. W., De Moortel, I., & De Pontieu, B. 2016, ApJL, 829, L18
Carlsson, M., Hansteen, V. H., de Pontieu, B., et al. 2007, PASJ, 59, S663
David, C., Gabriel, A. H., Bely-Dubau, F., et al. 1998, A&A., 336, L90
De Moortel, I. 2009, Space Science Reviews, 149, 65. http://dx.doi.org/10.1007/s11214-009-9526-5
De Moortel, I., Antolin, P., & Van Doorsselaere, T. 2015, SoPh, 290, 399
De Moortel, I., Ireland, J., Hood, A. W., & Walsh, R. W. 2002, A&A, 387, L13
De Pontieu, B., Erdélyi, R., & Moortel, I. D. 2005, The Astrophysical Journal Letters, 624, L61. http://stacks.iop.org/1538-4357/624/i=1/a=L61
De Pontieu, B., Hansteen, V. H., van der Voort, L. R., van Noort, M., & Carlsson, M. 2007, The Astrophysical Journal, 655, 624. http://stacks.iop.org/0004-637X/655/i=1/a=624
De Pontieu, B., McIntosh, S. W., Carlsson, M., et al. 2007, Science, 318, 1574
De Pontieu, B., McIntosh, S. W., Carlsson, M., et al. 2011, Science, 331, 55. http://science.sciencemag.org/content/331/6013/55
De Pontieu, B., Rouppe van der Voort, L., McIntosh, S. W., et al. 2014, Science, 346, 1255732
De Pontieu B., De Moortel I., Martinez-Sykora J., McIntosh S. W., 2017, ApJ, 845, L18
Del Zanna, G. 2013, A&A., 558, A73
Druckmüller, M. 2013, ApJS, 207, 25
Feng, X. S., & Xiang, C. Q. 2013, Sci Sin-Terrae, 43, 912
Feng, X. S., Xiang, C. Q., & Zhong, D. K. 2011, Sci Sin-Terrae, 41, 1
Fisher, G. H., & Welsch, B. T. 2008, in Astronomical Society of the Pacific Conference Series, Vol. 383, Subsurface and Atmospheric Influences on Solar Activity, ed. R. Howe, R. W. Komm, K. S. Balasubramaniam, & G. J. D. Petrie, 373
Habbal, S. R., Druckmüller, M., Morgan, H., et al. 2010a, ApJ, 719, 1362
—. 2010b, ApJ, 708, 1650
Hahn, M., Landi, E., & Savin, D. W. 2011, ApJ, 736, 101
Hahn, M., & Savin, D. W. 2014, ApJ, 795, 111
Hansteen, V., Guerreiro, N., De Pontieu, B., & Carlsson, M. 2015, ApJ, 811, 106
Henriques, V. M. J., Kuridze, D., Mathioudakis, M., & Keenan, F. P. 2016, ApJ, 820, 124
Howard, R. F., Harvey, J. W., & Forgach, S. 1990, SoPh, 130, 295
Ireland, J., McAteer, R. T. J., & Inglis, A. R. 2015, ApJ, 798, 1
Jess, D. B., Mathioudakis, M., Erdélyi, R., et al. 2009, Science, 323, 1582
Kleint, L., & Gandorfer, A. 2017, SSRv, 210, 397
Klimchuk, J. A. 2006, SoPh, 234, 41
Klimchuk, J. A., & Bradshaw, S. J. 2014, ApJ, 791, 60
Krishna Prasad, S., Jess, D. B., Klimchuk, J. A., & Banerjee, D. 2017, ApJ, 834, 103
Langangen, Ø., Carlsson, M., Rouppe van der Voort, L., Hansteen, V., & De Pontieu, B. 2008, ApJ, 673, 1194
Lemen, J. R., Title, A. M., Akin, D. J., et al. 2012, Solar Physics, 275, 17
Li, X., Morgan, H., Leonard, D., & Jeska, L. 2012, ApJLetters, 752, L22
Lin, H., Kuhn, J. R., & Coulter, R. 2004, ApJL, 613, L177
Lucas, B. D., & Kanade, T. 1981, in Proceedings of the 7th International Joint Conference on Artificial Intelligence - Volume 2, IJCAI'81 (San Francisco, CA, USA: Morgan Kaufmann Publishers Inc.), 674–679. http://dl.acm.org/citation.cfm?id=1623264.1623280
Mackovjak, Š., Dzifčáková, E., & Dudík, J. 2014, A&A., 564, A130
Mandal S., Samanta T., Banerjee D., Krishna Prasad S., Teriaca L., 2015, RAA, 15, 1832
McIntosh, S. W., de Pontieu, B., Carlsson, M., et al. 2011, Nature, 475, 477
Mendoza-Briceño, C. A., & Erdélyi, R. 2006, ApJ, 648, 722
Morgan, H. 2011, ApJ, 738, 189
Morgan, H., Byrne, J. P., & Habbal, S. R. 2012, ApJ, 752, 144
Morgan, H., & Druckmüller, M. 2014, Solar Physics, 289, 2945

Morgan, H., Jeska, L., & Leonard, D. 2013, ApJSupp., 206, 19

Pant, V., Dolla, L., Mazumder, R., et al. 2015, The Astrophysical Journal, 807, 71. http://stacks.iop.org/0004-637X/807/i=1/a=71

Parker, E. N. 1988, ApJ, 330, 474

Parnell, C. E., & De Moortel, I. 2012, Philosophical Transactions of the Royal Society of London Series A, 370, 3217

Pesnell, W. D., Thompson, B. J., & Chamberlin, P. C. 2012, Solar Physics, 275, 3

Plowman, J. 2016, Journal of Space Weather and Space Climate, 6, A8

Raouafi, N. E., Patsourakos, S., Pariat, E., et al. 2016, Space Science Reviews, 201, 1. http://dx.doi.org/10.1007/s11214-016-0260-5

Schrijver, C. J. 2001, SoPh, 198, 325

Sheeley N. R., Jr., Warren H. P., Lee J., Chung S., Katz J., Namkung M., 2014, ApJ, 797, 131

Skogsrud, H., van der Voort, L. R., & Pontieu, B. D. 2016, The Astrophysical Journal, 817, 124. http://stacks.iop.org/0004-637X/817/i=2/a=124

Starck, J.-L., Murtagh, F. D., & Bijaoui, A. 1998, Image processing and data analysis: the multiscale approach (Cambridge University Press)

Stenborg, G., & Cobelli, P. J. 2003, A&A, 398, 1185

Stenborg G., Marsch E., Vourlidas A., Howard R., Baldwin K., 2011, A&A, 526, A58

Sterling, A. C. 2000, Solar Physics, 196, 79. http://dx.doi.org/10.1023/A:1005213923962

Thurgood, J. O., Morton, R. J., & McLaughlin, J. A. 2014, ApJL, 790, L2

Tsiropoula, G., Tziotziou, K., Kontogiannis, I., et al. 2012, SSRv, 169, 181

Verwichte, E., Marsh, M., Foullon, C., et al. 2010, The Astrophysical Journal Letters, 724, L194. http://stacks.iop.org/2041-8205/724/i=2/a=L194

Wang T. J., Ofman L., Davila J. M., 2009, ApJ, 696, 1448

Withbroe, G. L., & Noyes, R. W. 1977, ARA&A, 15, 363

Wu, S. T., & Dryer, M. 2015, Science China: Earth Science, 58, 839

Zaqarashvili, T. V., & Erdélyi, R. 2009, SSRv, 149, 355

APPENDIX

.1. *Adapted Lucas-Kanade analysis: Method & Test*

This Appendix describes the LK method and validates the approach using test data. Motion of objects in image sequences is estimated by assuming that the temporal change in image brightness is due solely to the motion. Thus the x and y derivatives of image brightness are equated to the time derivative by:

$$\frac{\Delta I}{\Delta x} v_x + \frac{\Delta I}{\Delta y} v_y = -\frac{\Delta I}{\Delta t}, \tag{1}$$

where v_x and v_y are the x and y components of velocity, and I is the image brightness. For a given region in the image, the spatial and temporal derivatives of brightness are calculated for the local group of pixels, and the velocities estimated through least-squares. Typically, a Gaussian weighting centered on the pixel of interest is used, and the process repeated at each pixel, thus the velocity is mapped throughout the image. The method can suffer near the image edges (where the Gaussian-weighted local region is curtailed). Direct application of the method, without further adaptation (e.g. iterative approaches), is also insensitive to motion larger than a pixel per time step.

To characterise motions in the processed solar images, we have developed an adapted LK method, where the x and y velocity fields are approximated by local analytical functions. The functions are in the form of a constant plus a sum of a low-order sin/cos product series in the $x - y$ image plane.

For an input image pair, taken at consecutive times t_0 and t_1, the spatial x derivative at pixel i, j is calculated by a central difference applied to the first image:

$$\frac{\Delta I_{i,j}}{\Delta x} = \frac{I_{i+1,j} - I_{i-1,j}}{2\Delta x}, \tag{2}$$

and similar for the y derivative. The first image subtracted from the second image gives the time derivative.

To calculate the velocity field throughout the whole image, a local group of pixels centered on a current pixel of interest is identified. The local group is a square subregion of the image of size $[n_x, n_y]$, typically a few tens of pixels in each dimension. Coordinates x' and y' are defined within the subregion as

$$x' = \frac{\pi i}{n_x - 1}, \quad i = 0, 1, 2...n_x - 1, \tag{3}$$

$$y' = \frac{\pi j}{n_y - 1}, \quad j = 0, 1, 2...n_y - 1. \tag{4}$$

For integers k_x and k_y, which specify the function order, we define $S_{k_x} = \sin(k_x x')$, $C_{k_x} = \cos(k_x x')$, $S_{k_y} = \sin(k_y y')$ and $C_{k_y} = \cos(k_y y')$. A sinusoidal basis function is given by

$$S(x, y) = C + \sum_{k_x=1}^{N} \sum_{k_y=1}^{N} s_{k_x,k_y}, \tag{5}$$

where C is a constant and

$$s_{k_x,k_y} = c_{k_x,k_y,0} C_{k_x} C_{k_y} + c_{k_x,k_y,1} S_{k_x} S_{k_y} + c_{k_x,k_y,2} S_{k_x} C_{k_y} + c_{k_x,k_y,3} C_{k_x} S_{k_y}. \quad (6)$$

Thus for each order pair k_x, k_y there are four coefficients $c_{k_x,k_y,0-3}$. For example, if we choose order $N = 2$, there are 2 orders in both the x and y dimensions ($k_x = 1, 2$ and $k_y = 1, 2$), each containing the combination of four sin/cos functions given by equation 6, giving 16 coefficients in total. Including the constant C from equation 5 gives 17 coefficients in total. For order N the total number of coefficients is given by $4N^2 + 1$.

v_x and v_y are each described by the basis function of equation 5, and the coefficients are found using weighted least squares applied to equation 1 to the local group of pixels. The weighting is determined by a Gaussian function of the distance of each pixel from the central pixel. Local velocity fields are thus estimated across the whole image by sliding the square subregion across the image, in small increments that allow large overlap between neighbouring subregions. After scanning the whole image, the velocity fields from separate subregions are combined using weighted means in overlapping regions (with weights defined by distance from subregion centers).

The procedure above describes one iteration which gives the current estimate of velocity. The estimated velocity field at each iteration is used to warp the second image (thus 'reversing' the estimated motion), and the fitting procedure applied to the warped image to find a new velocity field. This new field is summed to the previous velocity estimate, and the process repeated until convergence is achieved. This is usually within a few iterations and allows estimates of motion greater than a pixel per time step.

The approach of using analytical functions as a support for the estimated local velocity field requires only a small order number to equation 5: attempting to fit a larger region would require a larger order number to estimate a velocity field that varies at small spatial scales. For the results shown in this paper, we use order $N = 3$ (37 coefficients each for v_x and v_y). The subregions are defined by squares that encompass circular Gaussian functions of 1-σ widths of 35 pixels (for input images at twice the AIA/SDO full resolution). The subregion is moved across the image in increments of $\sim$30 pixels (at AIA half-resolution), and the resulting velocities recorded. At the image edges, the subregion is truncated appropriately. Iteration is terminated when the ratio of the current velocity field to the main velocity field drops below 0.01 (the ratio is calculated across the whole image, and the 3% percentile maximum used as the termination criteria). The method suffers from edge effects. In this paper, we simply discard the results along a narrow border at the image edges.

The method is tested on an input pair of images, with the second image warped by a known amount. The first input image is shown in figure 22a. It is a 193Å time-normalized image from the boxed region near central disk (shown in the lower left panel of figure 5), binned to 512×512 pixels (double the pixel size of the original AIA/SDO image). The second, warped image is shown in figure 22b. The x and y warps are shown in figures 22a and b respectively. The mean magnitude of the pixel shifts between the images (or 'velocity') is based on velocities at the Sun of the order of 100 km s^{-1}, a cadence of 12s, and a pixel size of 868 km. Random noise of amplitude 10% of the standard deviation of the original image is added to both input images. As with the solar data, prior to running the LK method, the amplitude of the highest-frequency spatial component is reduced through applying an *à trous* multiresolution decomposition to each image (Starck et al. 1998), and summing the resulting 5 lowest frequency components (discarding the highest frequency component).

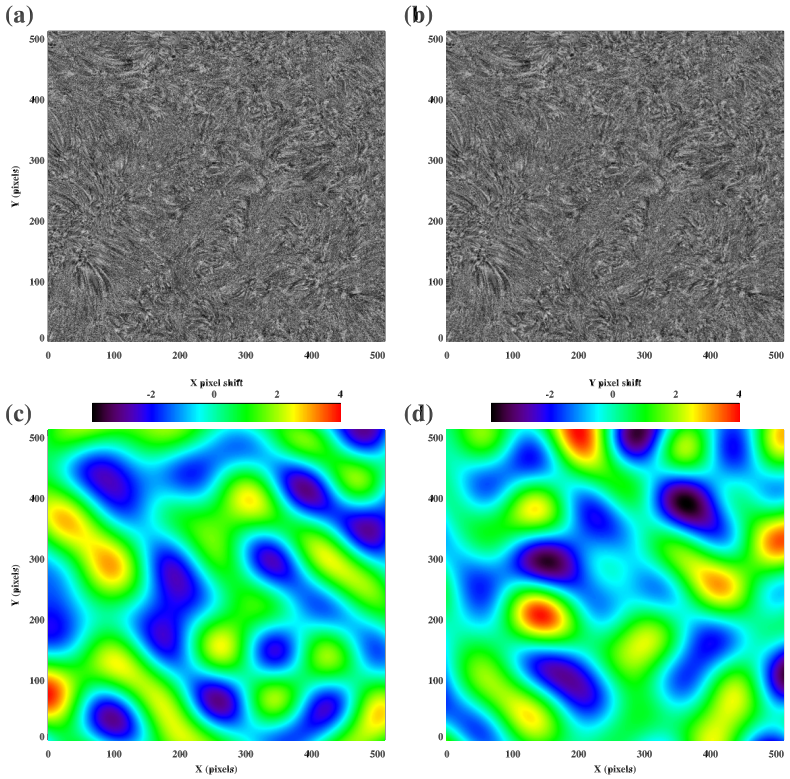

Figure 22. (a) First input image, (b) second input image (warped from the first), (c) x velocity field (or pixel shift between first and second images), (d) y velocity field.

Applying the adapted LK method as described leads to the results shown in figure 23. Despite the large amplitude of noise added to the test images, and the complicated velocity field, the method is robust. Figures 23a and b show the difference between the output and input pixel shifts in the x and y directions respectively. The maximum error is less than half a pixel (equating to ∼35 km s^{-1} in physical units). The good agreement is further shown in figures 23c and d, where slices of the x and y velocity components are compared across the center of the image. Figures 23e and f show histograms of the output minus the input velocities. The mean error is ∼0.08 pixels, equating to ∼6 km s^{-1} in physical units. Figures 23g and h show flow paths through the input and estimated velocity fields respectively.

.2. *Determining the wavelet power significance level*

The measure of significance in the wavelet power spectra is calculated using the following steps:

1. The initial discrete wavelet power spectrum of the input signal y is computed.

2. Based on a model of Gaussian-distributed noise, and a significance level of 96%, significant regions in the wavelet spectrum are identified. This follows the standard approach in wavelet analysis.

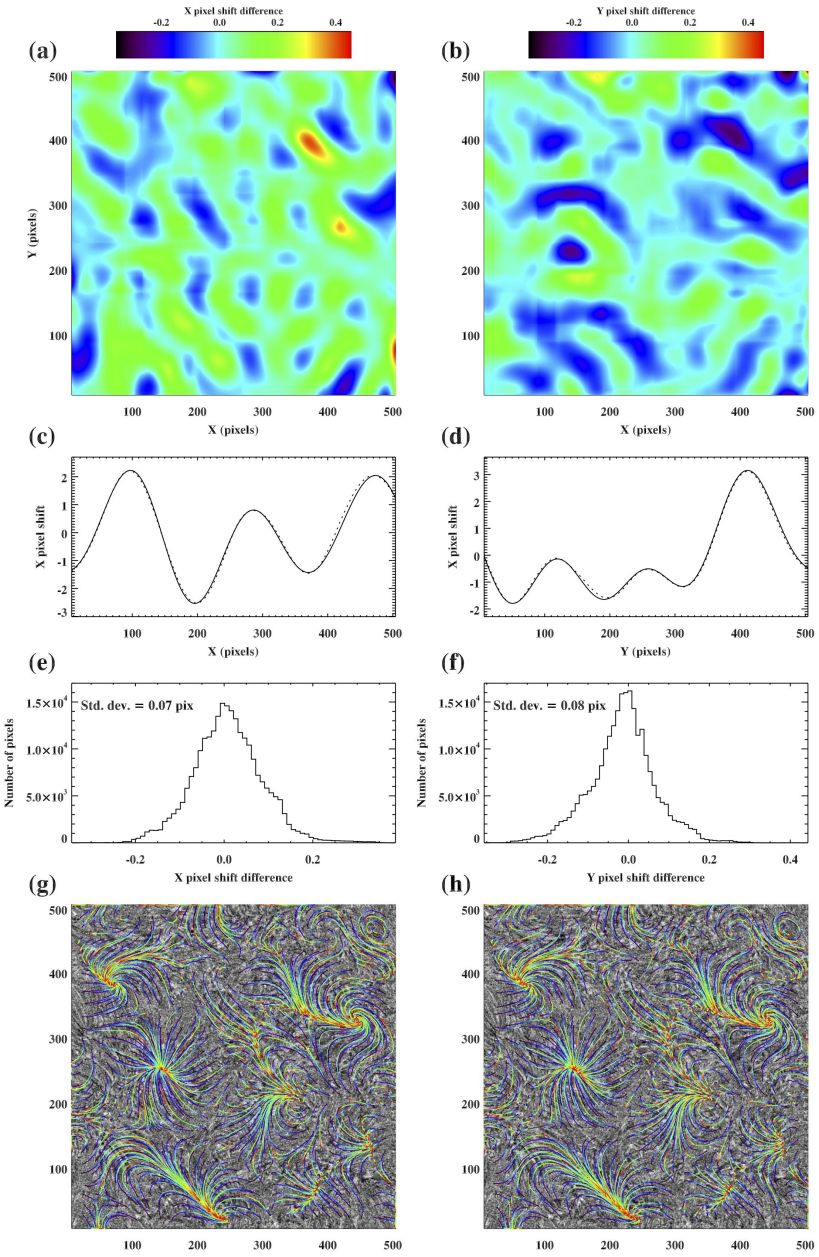

Figure 23. (a) Difference between the known input and LK-estimated x-pixel shift and (b) y-pixel shift. (c) A horizontal slice at $y = 256$ plotting the known input x-pixel shift (solid line) and LK-estimated (dotted). (d) As (c), but for the y-pixel shift. (e) Histogram of difference between estimated and true x-pixel shift. (f) as (e) but for the y-pixel shift. (g) Input pixel-shift (or velocity) field depicted as vectors, overlaid on the input image. Each colored path begins in blue from a random point, traces the velocity field, and ends in red. The colors enable a visualization of the local shift direction. (h) as (g) but for the estimated velocity field. Note that the boundaries of the images have been clipped (a strip of width 7 pixels discarded from each edge) due to unstable results at the edges.

3. The regions of significance of the wavelet spectrum are used to reconstruct a 'significant' signal y_s.

4. The residual signal is $y_r = y - y_s$.

5. The residual signal is 'scrambled' with a random index and added to y_s, and the wavelet power spectrum of the resulting signal calculated, along with regions of the spectrum which contain a significant oscillation. These are recorded.

6. The previous step is repeated 300 times. The mean power spectrum and mean significance level is calculated from these repetitions. Final significant oscillations are calculated from the mean wavelet power spectra and mean significant levels. The repetition allows, in principle, the calculation of uncertainties on the significance levels.

7. Finally, only regions of significance that last longer than a certain time period are kept. The threshold is set as a function of the periodicity, so significant oscillations will only be deemed significant if they last for longer than, for example, 3 whole oscillations.